

The UV spectrum of HS 1700+6416

II. FUSE observations of the He II Lyman alpha forest

C. Fechner¹, D. Reimers¹, G. A. Kriss², R. Baade¹, W. P. Blair³, M. L. Giroux⁴, R. F. Green⁵, H. W. Moos³, D. C. Morton⁶, J. E. Scott^{2,7}, J. M. Shull⁸, R. Simcoe⁹, A. Songaila¹⁰, and W. Zheng³

¹ Hamburger Sternwarte, Universität Hamburg, Gojenbergsweg 112, 21029 Hamburg, Germany,
e-mail: [cfechner, dreimers, rbaade]@hs.uni-hamburg.de

² Space Telescope Science Institute, 3700 San Martin Drive, Baltimore, MD 21218, USA, e-mail: gak@stsci.edu

³ Department of Physics & Astronomy, The Johns Hopkins University, 3400 North Charles Street, Baltimore, MD 21218, USA

⁴ Dept. of Physics, Astronomy, and Geology, East Tennessee State University, Johnson City, TN 37614, USA

⁵ Large Binocular Telescope Observatory, 933 N. Cherry, Tucson, AZ 85721, USA

⁶ Herzberg Institute of Astrophysics, National Research Council of Canada, 5071 West Saanich Road, Victoria, BC V9E 2E7, Canada

⁷ present address: Department of Physics, Astronomy, and Geosciences, Towson University, Towson, Maryland 21252, USA

⁸ CASA, Department of Astrophysical and Planetary Sciences, University of Colorado, Boulder, CO 80309, USA

⁹ MIT Center for Space Research, 77 Massachusetts Ave. 37-664B, Cambridge, MA 02139, USA

¹⁰ Institute for Astronomy, University of Hawaii, 2680 Woodlawn Drive, Honolulu, HI 96822, USA

Received February 1, 2006; accepted April 28, 2006

Abstract. We present the far-UV spectrum of the quasar HS 1700+6416 taken with FUSE. This QSO provides the second line of sight with the He II absorption resolved into a Ly α forest structure. Since HS 1700+6416 is slightly less redshifted ($z_{\text{em}} = 2.72$) than HE 2347-4342, we only probe the post-reionization phase of He II, seen in the evolution of the He II opacity, which is consistent with a simple power law. The He II/H I ratio η is estimated using a line profile-fitting procedure and an apparent optical depth approach, respectively. The expected metal line absorption in the far-UV is taken into account as well as molecular absorption of galactic H₂. About 27 % of the η values are affected by metal line absorption. In order to investigate the applicability of the analysis methods, we create simple artificial spectra based on the statistical properties of the H I Ly α forest. The analysis of the artificial data demonstrates that the apparent optical depth method as well as the line profile-fitting procedure lead to confident results for restricted data samples only ($0.01 \leq \tau_{\text{H}1} \leq 0.1$ and $12.0 \leq \log N_{\text{H}1} \leq 13.0$, respectively). The reasons are saturation in the case of the apparent optical depth and thermal line widths in the case of the profile fits. Furthermore, applying the methods to the unrestricted data set may mimic a correlation between the He II/H I ratio and the strength of the H I absorption. For the restricted data samples a scatter of 10 – 15 % in η would be expected even if the underlying value is constant. The observed scatter is significantly larger than expected, indicating that the intergalactic radiation background is indeed fluctuating. In the redshift range $2.58 < z < 2.72$, where the data quality is best, we find $\eta \sim 100$, suggesting a contribution of soft sources like galaxies to the UV background.

Key words. cosmology: observations – quasars: absorption lines – quasars: individual: HS 1700+6416

1. Introduction

The shape and the strength of the intergalactic UV background plays an important role in governing the evolution of the ionization state of the intergalactic medium (IGM). Since the IGM is observed to be highly ionized, ionization corrections have to be applied to measure properties of interest like its metallicity. The strength of the UV background, at least at the H I ionization edge, can be derived from the proximity effect (e.g. Scott et al. 2000), whereas more information is needed to con-

strain the shape of the ionizing radiation field. Agafonova et al. (2005) introduced a method to estimate the shape of the ionizing background from the observation of metal line absorbers.

Theoretical calculations model the shape of the UV background as the radiation of sources attenuated while propagating through the IGM. Quasars have been adopted as sources (Haardt & Madau 1996; Fardal et al. 1998) whose radiation has been filtered by the IGM. Since hydrogen and helium are the most abundant elements in the IGM, the resulting shape of the mean UV background is characterized by a sharp break at 1 Ryd and another break at 4 Ryd.

Observational results, however, suggest that the intergalactic UV background is dominated not only by the filtered radiation of quasars but also by a significant contribution from the softer radiation of galaxies. This evidence comes from the study of the H_I opacity (e.g. Kirkman et al. 2005) or the number density evolution of H_I absorbers (e.g. Zhang et al. 1997; Bianchi et al. 2001), and also the derivation of reasonable metallicities from observed metal line absorption requires softer radiation (Aguirre et al. 2004). Recent computations of the UV background therefore consider the contribution of galaxy radiation (e.g. Haardt & Madau 2001). Furthermore, Schaye (2004) and Miralda-Escudé (2005) pointed out that local sources may dominate over the mean background.

Besides H_I opacity measurements and the investigation of metal line systems, He_{II} provides another observational probe of the UV background. Comparing the strength of the He_{II} Ly α absorption to that of H_I leads to the column density ratio $\eta = N_{\text{He II}}/N_{\text{H I}}$, which is directly related to the ionizing background at the H_I and He_{II} photoionization edge (e.g. Fardal et al. 1998). Low values are expected for hard radiation, while high values should be measured if the ionizing radiation is dominated by soft sources. However, the observation of the He_{II} Ly α transition ($\lambda_{\text{rest}} = 303.7822 \text{ \AA}$) is very difficult. An unabsorbed, UV-bright QSO is needed at redshift $z \gtrsim 2$ to be observable with HST/STIS or FUSE (Picard & Jakobsen 1993). Up to now six of such quasars have been found (Jakobsen et al. 1994; Davidsen et al. 1996; Reimers et al. 1997; Anderson et al. 1999; Zheng et al. 2004a; Reimers et al. 2005a). Comparisons of the He_{II} opacity to the H_I opacity along a number of these sightlines point toward a dominant contribution to the ionizing UV background from hard sources, such as quasars, but with significant contributions also from soft sources such as star-forming galaxies (Heap et al. 2000; Kriss et al. 2001; Smette et al. 2002; Zheng et al. 2004a; Shull et al. 2004).

The He_{II} Ly α forest has been resolved for the first time towards the quasar HE 2347-4342 with FUSE (Kriss et al. 2001; Shull et al. 2004; Zheng et al. 2004b). Different analysis methods have been applied to derive the column density ratio (line profile fitting was used by Kriss et al. (2001) and Zheng et al. (2004b), while Shull et al. (2004) applied an apparent optical depth method) and lead to the same results: The UV background is highly variable on small scales with a fluctuation of the column density ratio between $1 \lesssim \eta \lesssim 1000$ or even more. Additionally, Shull et al. (2004) find an apparent correlation between the η value and the strength of the H_I absorption in the sense, that η appears to be larger in voids.

In this work we present FUSE observations of the quasar HS 1700+6416, which provides the second line of sight of a resolved He_{II} Ly α forest. Owing to the variability of the UV flux of this QSO (Reimers et al. 2005b), the data is of comparable quality like those of HE 2347-4342 ($S/N \sim 5$, $R \approx 20\,000$). The emission line redshift of HS 1700+6416 is $z_{\text{em}} = 2.72$, i.e. this line of sight probes the post-reionization universe, while in the spectrum of HE 2347-4342 the end of the He_{II} reionization phase has been detected (Reimers et al. 1997). HS 1700+6416 has a rich metal line spectrum in the optical as well as in the UV comprising seven Lyman

limit systems (LLS), which has been analyzed by several authors (e.g. Reimers et al. 1992; Vogel & Reimers 1993, 1995; Köhler et al. 1996; Petitjean et al. 1996; Tripp et al. 1997; Simcoe et al. 2002, 2006). Thus, metal line absorption features are also expected to arise in the far-UV polluting the Ly α forest absorption. Therefore, we will include a model of the metal line absorption in the analysis to obtain unbiased results. For this purpose, we derived a prediction of the metal line spectrum in the far-UV (Fechner et al. 2006), which we will consider in this work.

This paper is organized as follows: After presenting the observations in Sect. 2 and describing the extrapolation of the continuum for the FUSE spectral range in Sect. 3, we present the far-UV metal line prediction derived in Fechner et al. (2006) in Sect. 4 and give a comparison to the data. In Sect. 5 we discuss our artificial data and analyze them using the line profile-fitting procedure and the apparent optical depth method to investigate the applicability of these methods. The results derived from the observed data are presented and discussed in Sect. 6. We conclude in Sect. 7.

2. Observations

The Far Ultraviolet Spectroscopic Explorer (FUSE) uses four independent optical channels to enable high-resolution spectroscopy in the far-ultraviolet wavelength range below 1200 \AA . In each channel a primary mirror gathers light for a Rowland-circle spectrograph. Two-dimensional photon-counting detectors record the dispersed spectra. Two of the optical channels use LiF coatings on the optics to cover the 990 – 1187 \AA wavelength range. The other two channels cover shorter wavelengths down to 912 \AA using SiC-coated optics. Moos et al. (2000) give a full description of FUSE, and Sahnow et al. (2000) summarize its in-flight performance.

We observed HS 1700+6416 with FUSE through the 30"-square low-resolution apertures (LWRs) during four epochs in October 1999, May 2002, February/March 2003, and May 2003. Table 1 gives details of the individual observations. Between the exposures in May 2002 and 2003 the UV brightness of HS 1700+6416 increased by a factor ~ 3 (see Reimers et al. 2005b). Therefore, the final data are of better quality than we originally expected. The total exposure time is roughly 791 118 s with 290 230 s during orbital night.

We use the FUSE calibration pipeline CALFUSE V2.2.1 to process the data. The earliest versions of the calibration pipeline are described by Sahnow et al. (2000). CALFUSE V2.2.1 is described in detail on the FUSE web site (http://fuse.pha.jhu.edu/analysis/pipeline_reference.html). The major improvements to the pipeline since the description of Sahnow et al. (2000) that are relevant for our work are that data screening for bursts has been automated, and that a two-dimensional, multicomponent model for the background has been implemented. The background model takes into account the uniform (but time-varying) particle background in the detector as well as the spatially varying and time-varying portions of the background due to scattered light within the instrument.

Since we are working at the very limits of instrument sensitivity, we take additional non-standard steps in our process-

Table 1. Log of FUSE Observations of HS1700+64

| Observation ID | Date | t_{total} (s) | t_{night} (s) |
|----------------|-------------|------------------------|------------------------|
| P1100401 | 1999 Oct 14 | 57 038 | 23 275 |
| C1230101 | 2002 May 15 | 54 710 | 17 702 |
| C1230102 | 2002 May 16 | 53 821 | 15 663 |
| C1230103 | 2003 Feb 27 | 156 963 | 93 828 |
| C1230104 | 2003 Mar 03 | 130 605 | 51 584 |
| P3060101 | 2003 May 02 | 61 326 | 18 520 |
| P3060102 | 2003 May 03 | 57 952 | 17 863 |
| P3060103 | 2003 May 10 | 91 590 | 23 824 |
| Z0120101 | 2003 May 03 | 53 896 | 14 943 |
| Z0120102 | 2003 May 04 | 43 520 | 9 702 |
| Z0120103 | 2003 May 05 | 21 064 | 3 019 |
| Z0120104 | 2003 May 10 | 9 916 | 307 |

ing to reduce the background. We restrict the data to orbital night only (scattered light is ten times brighter during orbital day), and we select only detector events with pulse heights in the range 4 – 16. This reduces the background by an additional factor of two while still retaining photometric accuracy in the final result. Finally, since the instrument throughput is roughly a factor of three higher in the LiF channels compared to the SiC channels, we only use data from the LiF channels. The final spectrum therefore only covers the wavelength range 1000 – 1180 Å, with a gap at 1080 – 1086 Å due to the detector layout.

Each observation interval listed in Table 1 is processed separately. To assure the best spectral resolution and an accurate wavelength scale, we cross-correlate the overlapping wavelength regions of each extracted spectrum with each other. No wavelength shifts were identified that exceeded our final bin size of 0.05 Å. The extracted spectra from each detector segment and exposure are then merged onto a uniform wavelength scale in 0.05 Å bins. To maximize the resulting signal-to-noise ratio, each extracted spectrum is weighted by the product of the exposure time and the continuum flux at 1000 Å. This effectively weights each spectrum by the expected relative number of photons in each spectrum, which is the optimal weighting for data with Poisson-distributed errors. The resulting spectrum shown in Fig. 1 has $S/N \sim 5$ and a spectral resolution of $R \sim 20\,000$.

In the final merged spectrum we notice some potential problems with the zero flux level, particularly in the data at wavelengths shortward of 1080 Å. Strong, saturated H I absorption is detected at $z \approx 2.315$ and $z \approx 2.433$ arising from LLS at these redshifts. At the corresponding positions in the FUSE spectrum (~ 1007 Å and ~ 1043 Å) strong but slightly unsaturated features are detected. Since the column density ratio η should be > 1 because of physical plausibility, these features actually have to be saturated. However, the troughs of these presumably saturated lines are consistent with zero flux within the errors of our $S/N \sim 5$ spectrum. We note the systematic errors that may result from this in our future discussion, but note that data at longer wavelengths ($\lambda > 1086$ Å) does not appear to have the same problem. Saturated H I features at $z \sim 2.597$,

2.602, 2.634, and 2.683 show also saturated He II counterparts at ~ 1092 Å, 1094 Å, 1104 Å, and 1119 Å in the FUSE spectrum (see e.g. Fig 3). Thus, we are confident we can obtain unbiased results in the range $2.58 < z < 2.72$. Problems with the interpretation of the results due to inaccuracies in the zero flux level in the range $2.29 < z < 2.56$ will be discussed later.

The corresponding H I Ly α forest was observed with Keck. We have access to two datasets already published by Songaila (1998) and Simcoe et al. (2002). These two datasets are co-added obtaining a resulting spectrum with a total exposure time of 84 200 s and a signal-to-noise of $S/N \sim 100$ at 4000 Å. The co-added spectrum covers the wavelength range 3680 – 5880 Å with a resolution of $R \sim 38\,500$. The Simcoe data covers wavelengths down to ~ 3220 Å with less signal-to-noise. We also have used the absorption lines identified in this portion of the spectrum to constrain the metal line system models (see Fechner et al. 2006).

3. Continuum definition

In order to estimate the continuum in the FUSE portion of the spectrum we use low resolution data taken with HST/STIS in May 2003 simultaneously with the FUSE observations using the gratings G140L and G230L. The spectra cover the wavelength range 1150 – 3200 Å. The continuum is estimated considering galactic extinction, Lyman limit absorption, and the intrinsic spectral energy distribution of the QSO. Shortwards of the Lyman limit break the contribution of the optical depth of the LLS decreases due to the v^{-3} dependence of the hydrogen photoionization cross section. The strength of the break is proportional to the H I column density of the systems (see Møller & Jakobsen 1990), which have been measured by Vogel & Reimers (1995).

The galactic extinction towards HS 1700+6416 is about $E(B - V) = 0.025$ following Schlegel et al. (1998), whose values are based on dust maps created from COBE and IRAS infrared data. X-ray observations of this quasar carried out by Reimers et al. (1995) yield a hydrogen column density of $N_{\text{H}_1} = (2.9 \pm 1.3) \cdot 10^{20} \text{ cm}^{-2}$. Following Diplas & Savage (1994), this corresponds to $E(B - V) = 0.06$. Though the latter value is derived from direct observations of this line of sight, it is based on the measurement of H I only assuming a galaxy-wide gas-to-dust ratio, while Schlegel et al. (1998) use a combination of H I and the dust distribution. Therefore, we adopt the value $E(B - V) = 0.025$ from Schlegel et al. (1998).

The corrected flux is fitted with a power law $f_v \propto v^\alpha$ representing the intrinsic QSO continuum. The best fit succeeds using two power laws with a break at 2000 Å. The best fit yields $\alpha = -1.23$ at $\lambda < 2000$ Å and $\alpha = -1.54$ at $\lambda > 2000$ Å using the extinction curve of Cardelli et al. (1989). Comparing the STIS spectra to the FOS data analyzed by Vogel & Reimers (1995) taken in December 1991 the flux level is the same in the two datasets down to about 2000 Å. For this wavelength range the spectral index is in agreement with that derived from the older data. The continuum rises more steeply with decreasing wavelength in the FOS spectrum. At 1200 Å the flux level of the STIS data is depressed by a factor of about two in comparison to the FOS data. Between the two exposures in the course of

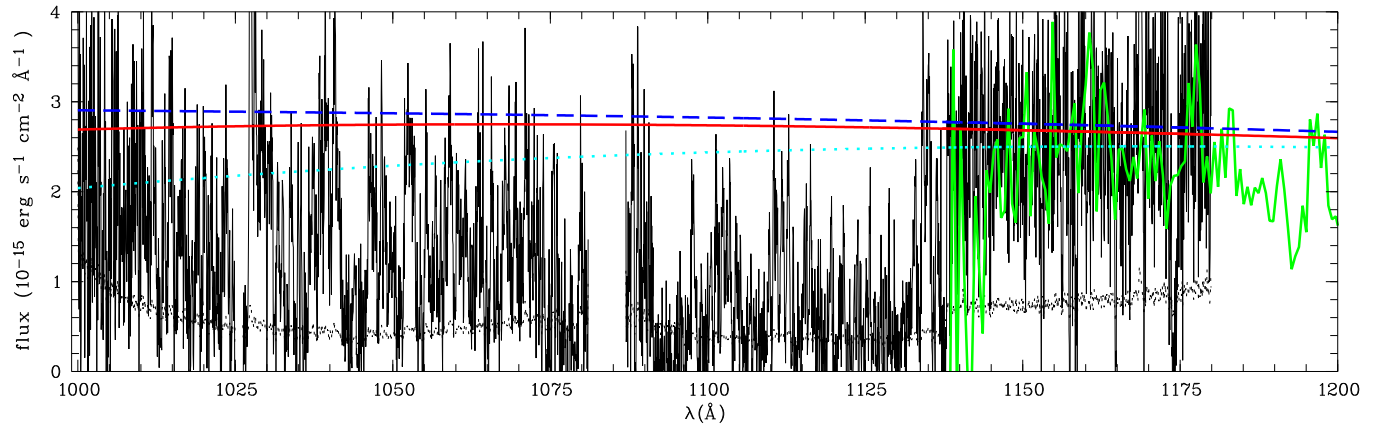


Fig. 1. The FUSE data and the extrapolated continuum. The solid line presents the continuum considering the Cardelli et al. (1989) extinction curve and $E(B - V) = 0.025$ (Schlegel et al. 1998). For comparison we show the extrapolated continuum using $E(B - V) = 0.060$ adopted from X-ray observations (Reimers et al. 1995) and the Cardelli et al. (1989, dotted line) or the Pei (1992, dashed line) extinction curve, respectively. Furthermore, we overlay the low resolution STIS data which was taken simultaneously with the FUSE data in May 2003. For a higher resolved presentation of the normalized FUSE spectrum see Fig. 3.

the observations with FUSE separated about a year, the quasar flux increased about a factor ~ 3 in the far-UV. This means HS 1700+6416 is highly variable in the intrinsic EUV even on relatively short time scales (Reimers et al. 2005b). Thus, in order to extrapolate a reliable continuum it is very important to have simultaneous STIS and FUSE observations. Fig. 1 illustrates that the FUSE and STIS portion of the spectrum taken in 2003 are well matched.

A crucial point in the continuum extrapolation is the choice of the extinction curve especially because of its steep rise in the UV. Adopting the analytic formula of Cardelli et al. (1989) we find a flux level at 1000 Å of $\sim 2.69 \cdot 10^{-15} \text{ erg s}^{-1} \text{ cm}^{-2} \text{ Å}^{-1}$. Tests with the reddening value derived from the X-ray observations (Reimers et al. 1995) lead to a flux at 1000 Å depressed by $\sim 25\%$ (see Fig. 1). Adopting the analytical expression of Pei (1992) an the same reddening value leads to a flux level slightly above the original extrapolation. But since the FUSE spectrum is extremely noisy especially in the lower wavelength range, the dominating uncertainties result from the profile fitting. The choice of the flux level affects the results only marginally. The apparent optical depth method is more sensitive to the continuum level. Adopting the normalization according to the lower continuum level given in Fig. 1 would lower the η values of individual bins by roughly 0.2 dex near 1000 Å. However, we are confident that the continuum extrapolation using the Cardelli et al. (1989) extinction curve and the $E(B - V)$ from Schlegel et al. (1998) represents a reasonable approximation of the real continuum.

The continuum in the Keck portion of the spectrum is estimated in the course of the line profile-fitting procedure. The line-fitting program CANDALF developed by R. Baade performs the Doppler profile fit and the continuum normalization simultaneously. Thus, the continuum determination in the Ly α forest is more reliable in comparison to an a priori continuum definition. The normalized Keck spectrum in the wavelength range corresponding to the He II data is shown in Fig. 2.

4. Metal line absorption

The spectrum of HS 1700+6416 is characterized by a large number of metal line absorption features in the optical spectral range (Petitjean et al. 1996; Tripp et al. 1997; Simcoe et al. 2002, 2006) as well as in the UV (Reimers et al. 1992; Vogel & Reimers 1993, 1995; Köhler et al. 1996). Since a significant contribution of absorption by metals is supposed to be present even in the far-UV, the expected metal lines in the FUSE portion have to be taken into account. Therefore, in the first paper of this series (Fechner et al. 2006) we construct photoionization models of the metal line systems with the main purpose to derive a prediction of the metal line features expected to arise in the FUSE spectral range. In the following the main results of Fechner et al. (2006) are summarized and we compare the predicted far-UV metal lines to the FUSE data. For details of the modelling procedure we refer to Fechner et al. (2006).

On the basis of the modelled column densities a metal line spectrum for the wavelength range 1000 – 1180 Å covered by FUSE is predicted. These lines (cf. Fig. 7 of Fechner et al. 2006) are overlayed to the observed FUSE data in Fig. 3. It can be seen, that some rather strong features can be identified as metal lines. Obviously, the prediction is consistent with the data for most of the lines.

In case of the LLS at $z = 0.8643$, however, strong features of oxygen are predicted, but the observed spectrum shows less absorption. In particular, O IV is overestimated, as can be seen at ~ 1032 Å and 1134 Å in Fig. 3. The model of this system is based on the Haardt & Madau (2001, HM) UV background. However, the spectral energy distribution of a starburst galaxy adopted from Bruzual A. & Charlot (1993, SB) leads to a reasonable model as well (Fechner et al. 2006). Therefore, another prediction is computed considering the results from the SB model for the $z = 0.8643$ system. The resulting metal line spectrum is also shown in Fig. 3. The main differences in the predicted lines are a decrease of the neon absorption (Ne III, Ne IV)

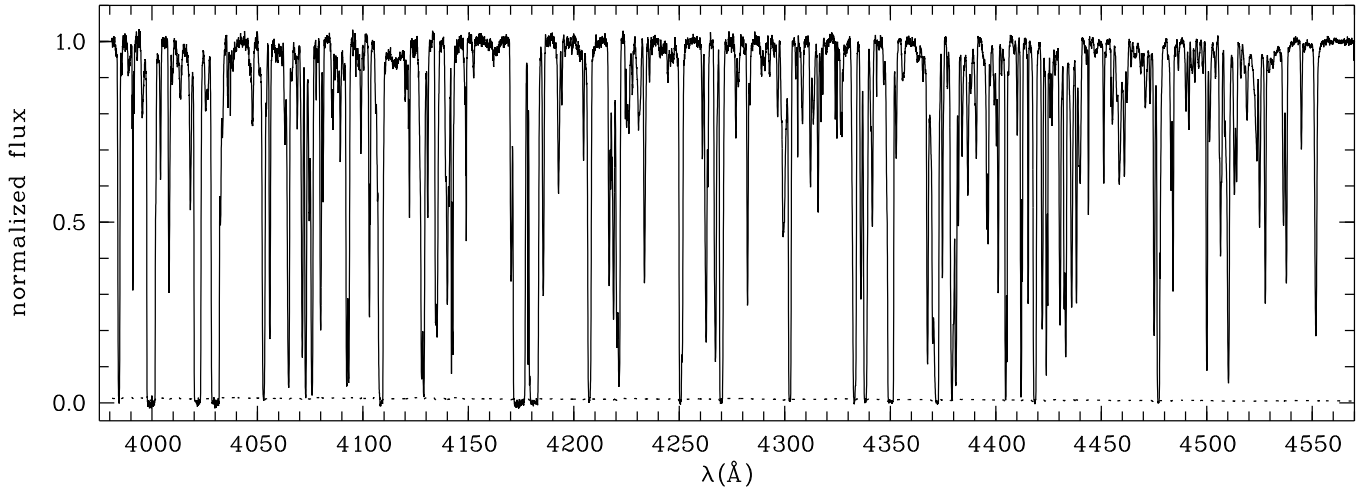


Fig. 2. The Keck data in the range $z > 2.27$. The data normalization is performed simultaneously with the estimation of the line parameters in course of the profile-fitting procedure.

in case of the SB model, but slightly stronger He I features. The predicted O IV features are consistent with the observed data. However, the strong feature at 1174 Å is mainly due to O V absorption from the $z = 0.8643$ system according to the HM model, while no O V absorption at all is predicted by the SB model. We find no alternative identification for this strong feature either proposed by the metal line system models or as part of the Lyman series of a strong, metal-free, low redshift system. Furthermore, no interstellar absorption line is expected at this wavelength. We conclude that also the energy distribution of a starburst galaxy does not provide an optimum model of the $z = 0.8643$ system. Improvement of the photoionization model by adopting a different ionizing background is difficult since only few transitions are observed in the optical. The vast majority of lines constraining the model are located in the UV, where the data suffers from low S/N (see also Fechner et al. 2006). When we analyze the He II Ly α forest taking into account the metal line prediction, we will reconsider the lines of the $z = 0.8643$ systems with different strengths dependent on the adopted model (especially those of Ne IV and Ne V) and discuss possible effects on the results.

Absorption from galactic molecular hydrogen is expected to arise additionally in the FUSE spectral range. Templates for the H₂ features with rest wavelengths in the far-UV including Lyman and Werner transitions and a detailed description of how to identify and eliminate them can be found in McCandliss (2003). Since the proposed procedure requires the detection of a sufficient number of undisturbed galactic H₂ features, it is inapplicable to our data. Instead, we proceed as follows: The templates from McCandliss (2003) are used to easily identify H₂ lines, considering that they may be slightly shifted in velocity space. Then, we select unblended features in the FUSE spectrum and fit them with Doppler profiles to estimate the line parameters. The selected transitions and the fitted line parameters are given in Table 2. All considered rotational transitions (ground state to $J'' = 0, 1, 2, 3$) can be modelled with a Doppler parameter $b = 5.0$ at a velocity $v = -45.7 \text{ km s}^{-1}$. The derived column densities for every J'' are also listed in Table 2.

Table 2. Transitions of galactic H₂ that are observed unblended in the FUSE spectrum. The atomic data (rest wavelength λ_0 and oscillator strength f) are adopted from Abgrall et al. (1993a,b). The column density is estimated assuming $b = 5.0 \text{ km s}^{-1}$ and $v = -45.7 \text{ km s}^{-1}$.

| transition | λ_0 (Å) | f | $\log N$ |
|-----------------|-----------------|--------|------------------|
| L (3 – 0) R (0) | 1062.882 | 0.0178 | 16.00 ± 0.87 |
| L (8 – 0) R (1) | 1002.453 | 0.0183 | 17.83 ± 0.25 |
| L (3 – 0) R (1) | 1063.460 | 0.0119 | |
| W (0 – 0) R (2) | 1009.023 | 0.0156 | 14.72 ± 0.30 |
| W (0 – 0) Q (2) | 1010.938 | 0.0245 | |
| W (0 – 0) P (2) | 1012.170 | 0.0055 | |
| L (7 – 0) R (2) | 1014.977 | 0.0190 | |
| L (7 – 0) P (2) | 1016.458 | 0.0102 | |
| L (6 – 0) P (2) | 1028.106 | 0.0105 | |
| L (5 – 0) R (2) | 1038.686 | 0.0165 | |
| L (4 – 0) P (2) | 1053.283 | 0.0090 | |
| L (8 – 0) R (3) | 1006.413 | 0.0158 | 15.49 ± 0.30 |
| W (0 – 0) R (3) | 1010.129 | 0.0138 | |
| L (6 – 0) R (3) | 1028.983 | 0.0173 | |
| L (5 – 0) R (3) | 1041.157 | 0.0159 | |

Because of the few observed unblended lines and the poor data quality, the column densities, especially those of the lower rotational transitions, are very uncertain. Nevertheless, the derived values are roughly consistent with the column densities derived by Richter et al. (2001, 2003) for high- and intermediate-velocity clouds, respectively, towards extragalactic sources. In the final step, all transitions within the observed spectral range with $J'' = 0, 1, 2, 3$ are included into our model.

In the following we treat the H₂ model like the predicted metal absorption lines. Unless explicitly noted we refer to the predicted metal line absorption as well as galactic H₂ when talking about metal lines. Using either the profile-fitting procedure or the apparent optical depth method all additional lines

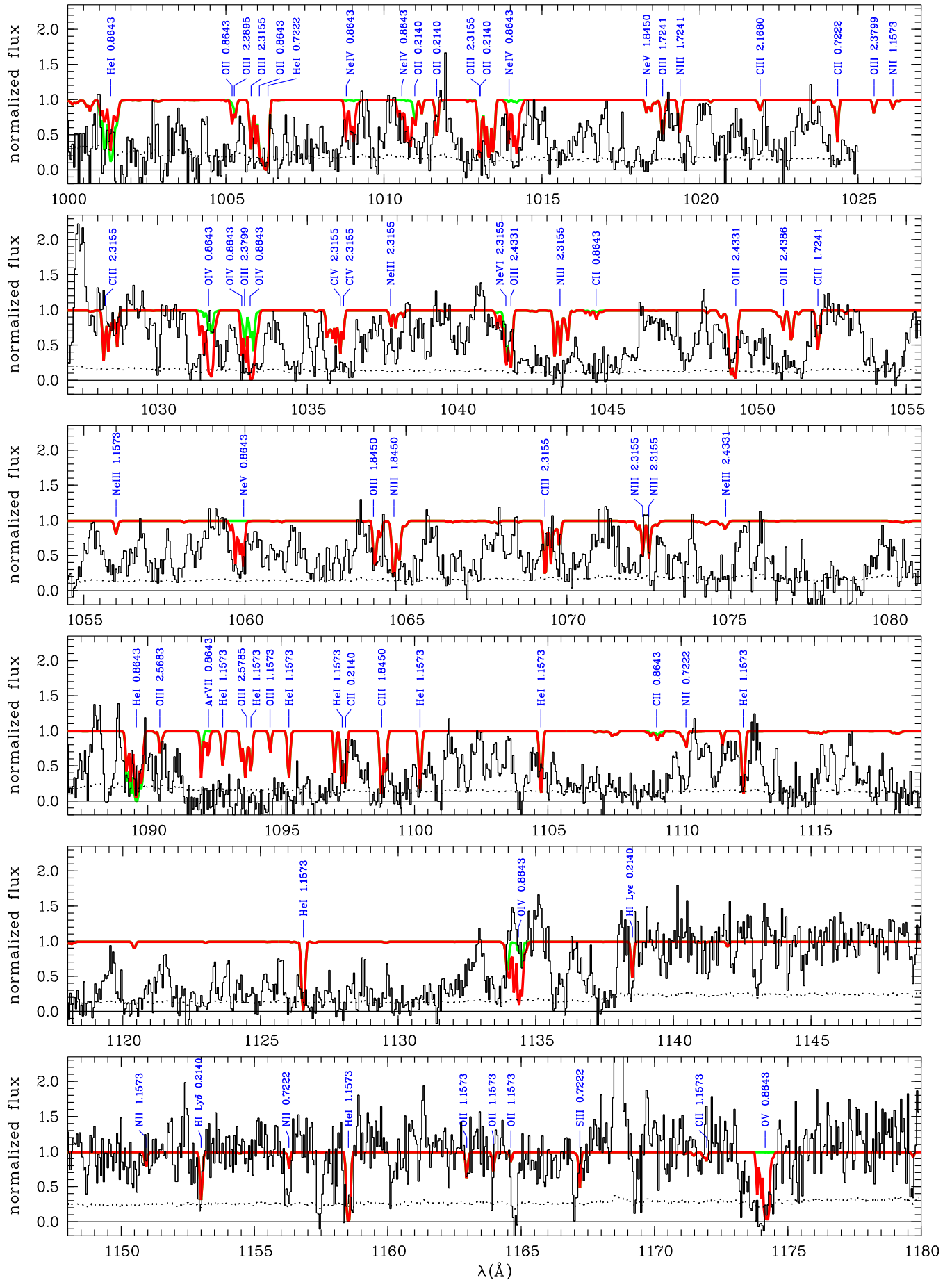


Fig. 3. Predicted metal line spectrum (smooth solid line) in comparison to the data (histogram-like solid line). The dotted line represents the error of the observational data. The predicted features are identified given the ion and the redshift of the system where they arise.

are considered in the analysis of the He II Ly α forest. Besides the metal lines also the interstellar lines C II λ 1036 and Ar I $\lambda\lambda$ 1048, 1067 are included.

We roughly estimate how strongly the FUSE spectral range might be affected by lines of the higher Lyman series lines of the H I Ly α forest at $z \lesssim 0.2$. The model spectrum derived in Fechner et al. (2006) is compared to the STIS UV data covering the wavelength range 1230 – 1550 Å used to constrain the models. Assuming all unidentified, strong features are low redshift Ly α lines, the expected positions of the higher order Lyman series lines are computed. Most of the systems are not expected to contribute to the absorption in the FUSE spectral range since higher order Lyman series lines located redwards of the He II forest are detected only very weakly. However, three systems at $z = 0.1240, 0.0809$, and 0.0237 possibly affect the He II Ly α forest. The Ly β feature of the system at $z = 0.1240$ is blended with Ly δ of the metal line system at $z = 0.2140$ both located at ~ 1153 Å. The corresponding Ly γ and δ features are expected at 1093.1 Å and 1067.5 Å, respectively. From the system at $z = 0.0809$ absorption is expected at 1108.7 Å (Ly β) and 1051.2 Å (Ly γ), while the Ly β features of the $z = 0.0237$ systems should be located at 1050.0 Å. As can be seen from Fig. 4, no remarkably high η values are detected at $z \sim 2.456, 2.460, 2.514$, and 2.650 , corresponding to the wavelength positions discussed above. Therefore, biases in η due to higher order Lyman series lines of the low redshift H I forest should be negligible.

The importance of metal line absorption in the FUSE spectral range is illustrated in Fig. 4. The upper panel shows the redshift distribution of η estimated by fitting Doppler profiles to the H I and He II Ly α forest ignoring metal line absorption (for details of the analysis procedure see Sect. 5.1), while metal line features have been considered in the lower panel. Lower limits indicate He II absorbers without detected H I counterpart. About 32 % of the apparent He II features have no H I counterpart when metal line absorption is ignored. The consideration of metal lines reduces the number of lower limits significantly, since several absorption features can be identified as metal lines. In this case only 25 % additional He II lines are needed. Data points that have been biased by metal line absorption, are marked in the lower panel of Fig. 4. In total roughly 27 % of the measured values are affected. For 19 % of the data points, η changes by more than $\Delta \log \eta = 0.01$ when extra absorption is taken into account. Considering only features of galactic H₂, about 6 % of the data points would have been biased, i.e. the major contribution comes from the predicted metal line absorption. There are no indications of unusually high column density ratios at the position of metal lines arising from the $z = 0.8643$ system.

The median column density ratio decreases from $\log \eta = 1.99$ if metal lines are neglected to 1.93 if they are taken into account. Consequently, the consideration of metal line absorption has no severe influence on the general statistical properties of the η distribution. The column density ratio of a single absorber, however, can be distorted up to an order of magnitude.

5. Simulations

Two different methods have been used so far to analyze the data of the He II Ly α forest towards HE 2347-4342. Kriss et al. (2001) and Zheng et al. (2004b) fit line profiles to the observed absorption features. The use of profile fits assumes the absorption features to arise from discrete clouds in the IGM, which is certainly an oversimplification. The alternative method measuring the apparent optical depth was also applied to the HE 2347-4342 data (Shull et al. 2004). In this case the column density ratio η is estimated by the ratio of the He II and H I optical depth per redshift or velocity bin. Since η is defined per bin, the assumption of discrete absorbers can be dropped in favour of a continuous medium, where the features are due to density fluctuations. A third approach fitting the optical H I Ly α forest directly to the UV spectrum in order to derive η has been introduced by Fechner & Reimers (2006).

In order to study possible effects of the analysis method on the results we create artificial datasets. By evaluating the artificial spectra we investigate how the results are influenced by the applied method. For both methods we recognize problems which prevent the accurate reconstruction of the presumed η value. In the following we briefly summarize the methodical procedures, then describe the generation of the artificial data, and discuss the implications of the profile-fitting procedure and the difficulties using the apparent optical depth method.

5.1. Methods

In preparation of the profile fit of the He II spectrum, we first identify all H I Ly α features in the optical data and estimate their parameters by fitting Doppler profiles. In the case of strongly saturated Ly α lines higher orders of the Lyman series up to Ly ϵ are considered as well to derive the parameters. Then, the He II Ly α forest is fitted fixing the redshift and the Doppler parameter derived from the corresponding hydrogen lines. The latter constraint implies, that we assume pure turbulent broadening. Zheng et al. (2004b) made the attempt to derive the dominant broadening mechanism from the HE 2347-4342 data fitting unblended He II features with a free b -parameter. They found a velocity ratio $\xi = b_{\text{He}}/b_{\text{H}}$ close to 1.0, suggesting turbulent broadening to be dominant. However, Fechner & Reimers (2006) demonstrate that thermal broadening is important for part of the absorbers and can lead systematically to lower η values for high density H I absorbers.

The procedure of the apparent optical depth method applied to He II Ly α forest data as described by Shull et al. (2004) will be summarized briefly: The column density ratio is replaced by $\eta = 4 \cdot \tau_{\text{He II}}/\tau_{\text{H I}}$ (Miralda-Escudé 1993, more exactly the factor 4 represents the ratio of the rest wavelengths $\lambda_{0, \text{H I}}/\lambda_{0, \text{He II}} = 1215.6701/303.7822$), where the optical depths $\tau = -\ln F$ are measured per bin. In order to obtain physically reasonable values, bins with normalized fluxes F above unity are masked out as well as bins with flux values below zero. Additionally, bins with flux values within 1σ from unity or zero are not considered, since they cannot be distinguished statistically from the continuum or zero, respectively.

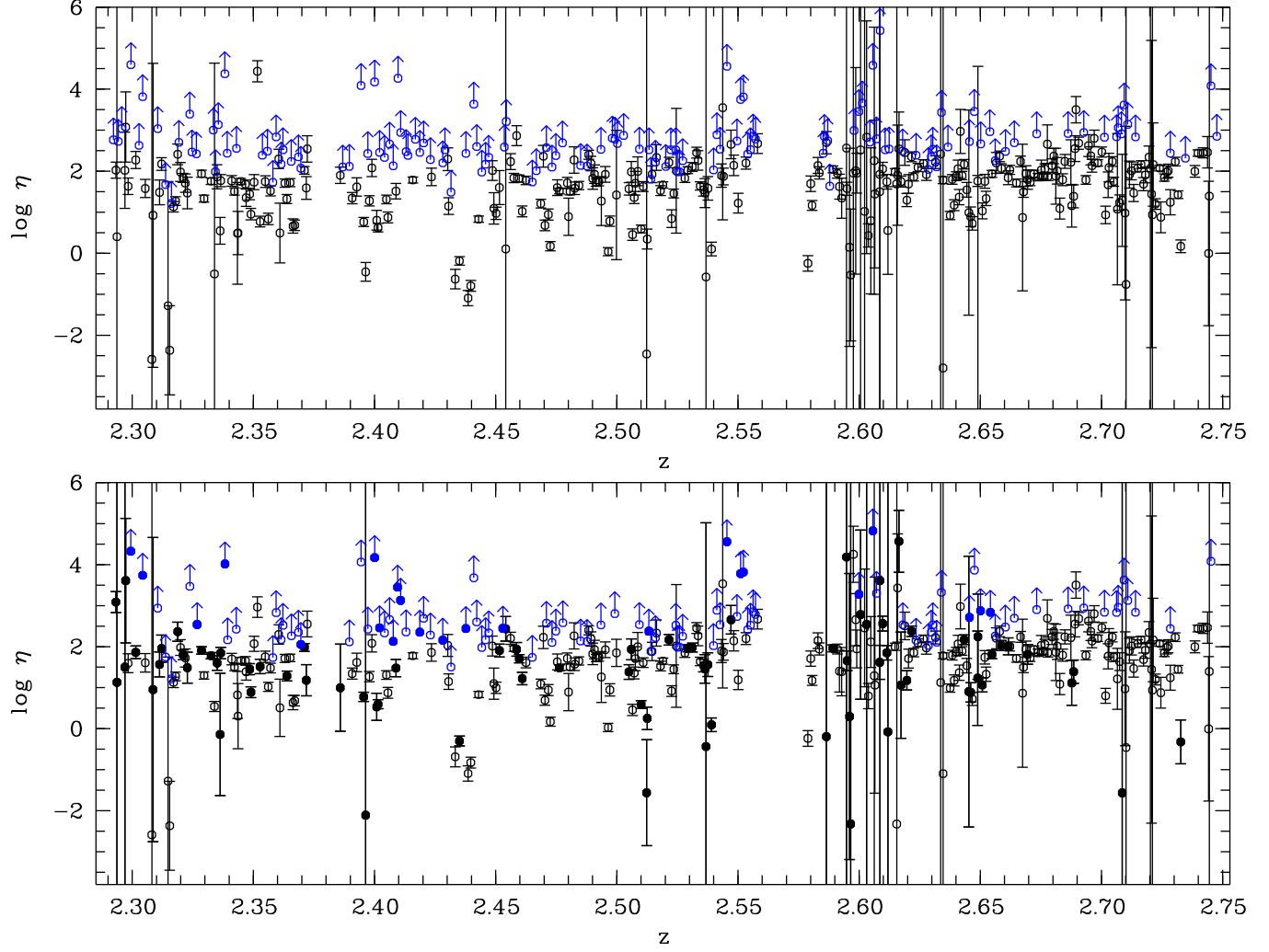


Fig. 4. Comparison of the $\eta(z)$ distribution ignoring metal line and galactic H₂ absorption (upper panel) and taking them into account (lower panel). Absorbers affected by extra absorption are marked as filled circles. Lower limits are based on He II features without detected H I counterparts. Their Doppler parameters are chosen to be $b = 27.0 \text{ km s}^{-1}$.

5.2. Creating artificial datasets

Based on the statistical properties of the H I Ly α forest as observed towards HS 1700+6416, a sample of lines is generated. The column density distribution function with $\beta = 1.5$ is adopted from Kirkman & Tytler (1997). Values in the range $11.0 \leq \log N \leq 18.0$ are simulated. Our observed line sample yields $\beta = 1.51 \pm 0.05$ for absorbers with $12.8 \leq \log N \leq 16.0$. The Doppler parameter distribution is described by a truncated Gaussian

$$\frac{dN(b)}{db} = \begin{cases} A \cdot \exp\left(-\frac{(b - b_0)^2}{2\sigma_b^2}\right) & b \geq b_{\min} \\ 0 & b < b_{\min} \end{cases}$$

with $b_0 = 27 \text{ km s}^{-1}$, $\sigma_b = 8.75 \text{ km s}^{-1}$, and $b_{\min} = 10 \text{ km s}^{-1}$ as observed towards HS 1700+6416 in good agreement with Hu et al. (1995). In addition, the parameters of the simulated line sample are correlated by $b_{\min} = (1.3 \cdot (\log N - 12.5) + 10.5) \text{ km s}^{-1}$ following Misawa (2002). The artificial spectrum covers the redshift range $2.292 < z < 2.555$, which corresponds

to wavelengths shorter than 1080 Å in the FUSE spectrum. No number density evolution is considered along this redshift interval. The minimal distance between two lines is $dz = 0.0001$ as observed towards HS 1700+6416. In the given redshift range the separation corresponds to $\sim 20 \text{ kpc}$. The resolution of $R = 40\,000$ and the signal-to-noise ratio of $S/N \sim 100$ are chosen to match the characteristics of high-resolution spectra taken with VLT/UVES or Keck/HIRES.

The He II Ly α forest is computed based on the artificial H I lines using $\eta = 80$, the mean value found by Kriss et al. (2001). Considering a temperature of 10^4 K the He II Doppler parameter is computed as

$$b_{\text{He II}} = \sqrt{b_{\text{H I}}^2 - 2kT\left(\frac{1}{m_{\text{H}}} - \frac{1}{m_{\text{He}}}\right)}. \quad (1)$$

The assumed temperature is cooler than the average $2 \cdot 10^4 \text{ K}$ measured by Ricotti et al. (2000), but consistent with $b_{\min, \text{H I}} = 10 \text{ km s}^{-1}$. Test calculations with higher temperatures indicate no difference in the results. Since the IGM is expected to

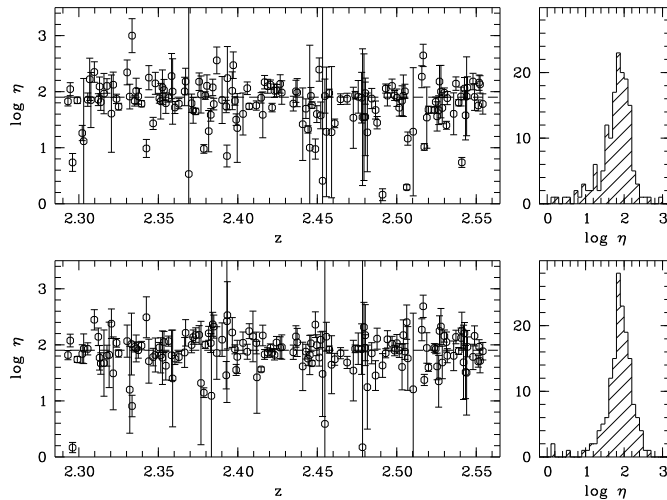


Fig. 5. Distributions of the column density ratio η derived from the artificial data with a Doppler parameter consisting of a thermal and a turbulent part (upper panel) or a pure turbulent b -parameter (lower panel) applying a profile-fitting procedure. The dashed line indicates the presumed value $\eta = 80$. In the course of the analysis pure turbulent broadening is assumed in both cases.

have a distinctive temperature distribution, a constant temperature model is certainly an oversimplification, but serves to get an impression of the possible effects assuming pure turbulent broadening. For comparison we compute as well a He II dataset with $b_{\text{He II}} = b_{\text{H I}}$. The resolution of $R = 15\,000$ and the signal-to-noise ratio of $S/N \sim 5$ are chosen to match the typical values of real FUSE data.

Since the artificial spectra are generated from statistical assumptions alone, they provide only a simple approach to investigate the applicability of the methods. More realistic spectra based on hydrodynamical simulations are presented by Bolton et al. (2006). They find that the column density ratio can be estimated confidently by a line profile-fitting procedure (but see discussion below and in Fechner & Reimers 2006). Furthermore, their simulations permit the investigation of different UV backgrounds, whereas the simple statistical approach introduced here can provide only limited information about basic problems of the analysis procedures.

5.3. Profile fitting analysis

Having analyzed the artificial H I Ly α forest by fitting Doppler profiles, the statistical properties of the sample are recovered. Under the simulated conditions our sample is complete down to $\log N \sim 12.0$. Due to blending effects, the deduced Doppler parameter distribution is broadened by 28 %. The He II Ly α forest lines are treated the same way, using the derived H I parameters, with fixed line redshifts and b -parameters. Features with Doppler parameters $b < 10 \text{ km s}^{-1}$ are not considered. The resulting η values are shown in Fig. 5. Both the combined thermal and turbulent as well as the pure turbulent broadened sample show a scatter in η of about 0.5 dex. Generally, the line sample that contains thermal broadening has more low η values. We

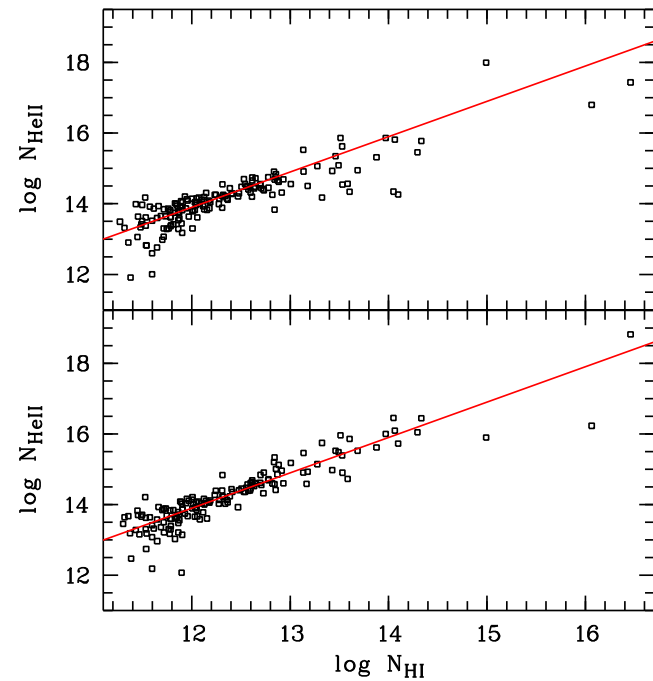


Fig. 6. Recovered He II column densities versus H I column densities for combined thermal and turbulent broadening (upper panel) and in the pure turbulent case (lower panel). The solid line represents the underlying correlation $\eta = 80$. For clarity, measurement errors are not plotted.

find a statistical mean of $\log \eta_{\text{therm}} = 1.77 \pm 0.43$ in comparison to $\log \eta_{\text{turb}} = 1.86 \pm 0.37$ in the pure turbulent case, both still consistent with the presumed value of 1.90309. The median, which gives less weight to outliers, is $\log \eta_{\text{therm}} = 1.86$ and $\log \eta_{\text{turb}} = 1.90$, respectively.

There are various reasons for outliers lying outside the range $\log \eta = 1.903 \pm 0.500$. Both models show only about 3 % high values caused by line saturation and blending effects, which can, in principle, produce low as well high η values. In the sample with pure turbulent broadening we find 8 % low η values while the thermal and turbulent broadened sample shows 14 % low values. Besides saturation and blending, the uncertainties of the parameters of weak H I lines resulting in large error bars are a primary reason. In the case of combined thermal and turbulent broadening some He II lines are narrower than the adopted pure turbulent b -parameter of H I. This effect produces about 25 % of the low values. Therefore, if the widths of intergalactic absorbers are not completely dominated by turbulent mechanisms, low η values can be caused by the assumption of pure turbulent broadening (see also Fechner & Reimers 2006).

In order to find a strategy for avoiding artificial scatter in the η distribution, we directly examine the correlation between H I and He II column density as presented in Fig. 6. The correlation fits well except for very low column densities ($\log N_{\text{H I}} < 12.0$) where noise makes it difficult to derive accurate line parameters, and also for high column densities, where saturation of hydrogen lines plays a role (features are saturated when $\log N_{\text{H I}} \gtrsim 14.5$ for $b \approx 27 \text{ km s}^{-1}$). Since the redshift

and Doppler parameter of the helium lines are fixed during the fitting procedure, the column densities are derived correctly if the underlying assumptions are correct. In the case of combined thermal and turbulent broadening the He II column densities are significantly underestimated for $\log N_{\text{H}_1} \gtrsim 13.0$, caused by the assumption of pure turbulent broadening. Fechner & Reimers (2006) argued that the incorrect assumption of pure turbulent broadening affects only lines above this H_1 column density. Thus, a stringent criterion to define a reasonable subsample would be $12.0 \leq \log N_{\text{H}_1} \leq 13.0$. Assuming pure turbulent broadening as a good approximation, $12.0 \leq \log N_{\text{H}_1} \leq 14.5$ provides a less stringent constraint.

Bolton et al. (2006) find a distribution similar to that shown in the lower panel of Fig. 6. Their lines samples contain only absorber with $\log N_{\text{H}_1} > 12.0$ and show enhanced scatter for $\log N_{\text{H}_1} > 13.0$ even in the case of a uniform UV background. Since they assumed turbulent broadening as well, the scatter most likely indicates the effect of thermal line widths. However, Bolton et al. (2006) neither discuss the origin of the scatter nor the possible implications of the assumption of pure turbulent broadened lines.

Applying the criteria derived above to the simulated datasets we find the statistical means $\log \eta_{\text{therm}} = 1.85 \pm 0.21$ and $\log \eta_{\text{turb}} = 1.92 \pm 0.21$ for the more stringent constraint ($12.0 \leq \log N_{\text{H}_1} \leq 13.0$). In the pure turbulent case, the underlying η value is recovered well, while it is still underestimated when thermal broadening plays a role. For both samples the statistical 1σ error has been reduced by a factor ~ 2 in comparison to the total sample. Considering the sample $12.0 \leq \log N_{\text{H}_1} \leq 14.5$ yields $\log \eta_{\text{therm}} = 1.74 \pm 0.39$ and $\log \eta_{\text{turb}} = 1.92 \pm 0.25$, respectively. Here, the underestimation of η for the data including thermal broadening gets worse and the scatter increases, while the mean value and 1σ error for the pure turbulent data do not change significantly.

5.4. Apparent optical depth method

The same artificial datasets are analyzed applying the apparent optical depth method. The resulting distribution for a bin size of $\Delta v = 20 \text{ km s}^{-1}$, corresponding to 0.05 \AA in He II wavelengths, is shown in Fig. 7. This method leads to a scatter in η of about 0.5 dex for both models as well. The high values are statistically negligible, since they are only about 3 % for each sample. Again we find slightly more low η values when thermal broadening is present (roughly 13 % in comparison to 10 % in the case of pure turbulent broadening). This is plausible, since the He II optical depth in the wings of a thermally broadened, and therefore narrower feature is systematically lower than in the case of pure turbulence. In both models the underlying η is underestimated. We find the mean values $\log \eta_{\text{therm}} = 1.80 \pm 0.44$ and $\log \eta_{\text{turb}} = 1.84 \pm 0.41$. With increased bin size the mean values get even lower ($\log \eta_{\text{therm}} = 1.75 \pm 0.39$ and $\log \eta_{\text{turb}} = 1.77 \pm 0.38$ for $\Delta v = 60 \text{ km s}^{-1}$, corresponding to a bin size of 0.20 \AA in He II). Also the median underestimates the real η in the combined broadening case because of the excess of low values, even though this effect is smaller. We find $\log \eta_{\text{therm}} = 1.88$

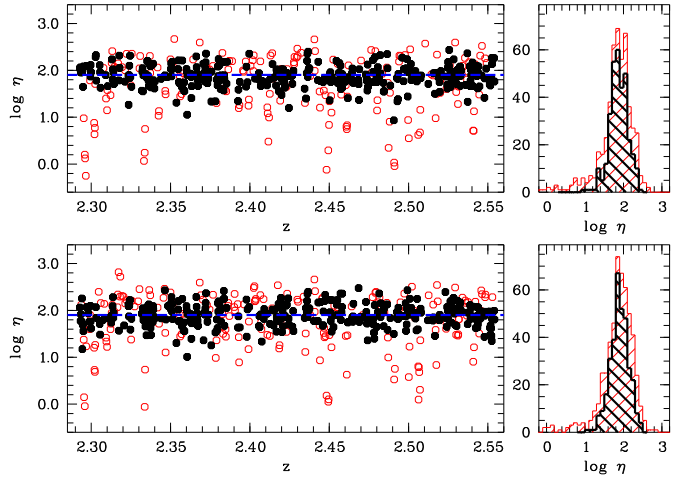


Fig. 7. Distributions of the column density ratio η derived from the artificial data with a Doppler parameter consisting of a thermal and a turbulent part (upper panel) or a pure turbulent b -parameter (lower panel) using the apparent optical depth method. The dashed line indicates the presumed value $\eta = 80$. The bin size is 20 km s^{-1} , corresponding to $\sim 0.05 \text{ \AA}$ in He II . Bins with $-2.0 \leq \log \tau_{\text{H}_1} \leq -1.0$ (see text) are denoted as filled circles, all others as open circles. The corresponding distributions are indicated as histograms in the right panels.

and $\log \eta_{\text{turb}} = 1.90$ (bin size 20 km s^{-1}), in comparison to $\log \eta_{\text{therm}} = 1.81$ and $\log \eta_{\text{turb}} = 1.83$ with 60 km s^{-1} bin size.

The correlation between low H_1 optical depth, referred to as voids, and high η values as found by Shull et al. (2004) can also be seen in the simulated data even though it is not present in the underlying spectra. For further investigation of this point it is instructive to regard η as the correlation between τ_{H_1} and $\tau_{\text{He II}}$. This is shown in Fig. 8 in the pure turbulent case for different signal-to-noise ratios of the He II data (100, 10, and 5, while $S/N = 100$ is constant for the H_1 spectra) and an example without any noise.

At the given S/N of the H_1 spectrum ($= 100$), optical depths down to $\log \tau_{\text{H}_1} > -2.0$ can be measured reliably, at least in principle. If only bins detached by more than 2σ from unity are considered, the limit is $\log \tau_{\text{H}_1} > -1.7$. The scatter at low optical depths (e.g. for $\log \tau_{\text{H}_1} \lesssim -1.7$ in the case of $S/N = 100$ for H_1 as well as He II) is due to the noise. In order to avoid a contamination by noise-affected bins, the constraints defining the subsample should be chosen carefully. As can be seen from Fig. 8, the detection limit of the He II optical depth depends on the signal-to-noise, of course. In case of $S/N = 5$ the restriction is $\log \tau_{\text{He II}} > -0.65$, or $\log \tau_{\text{He II}} > -0.3$ for the 2σ constraint.

Even the analysis of the spectra without noise leads to scatter around the underlying relation. Furthermore, bins with an optical depth above $\log \tau_{\text{H}_1} > -1.0$ (indicated by the vertical, dotted line in Fig. 8) yield He II optical depths clearly beneath the expected values. This flattening is due to line saturation, since saturated absorption features become broader and more smeared out at finite resolution. The difference in the profile does not only affect the saturated core but as well the wings of the line. Consequently, the flattening starts at relatively low

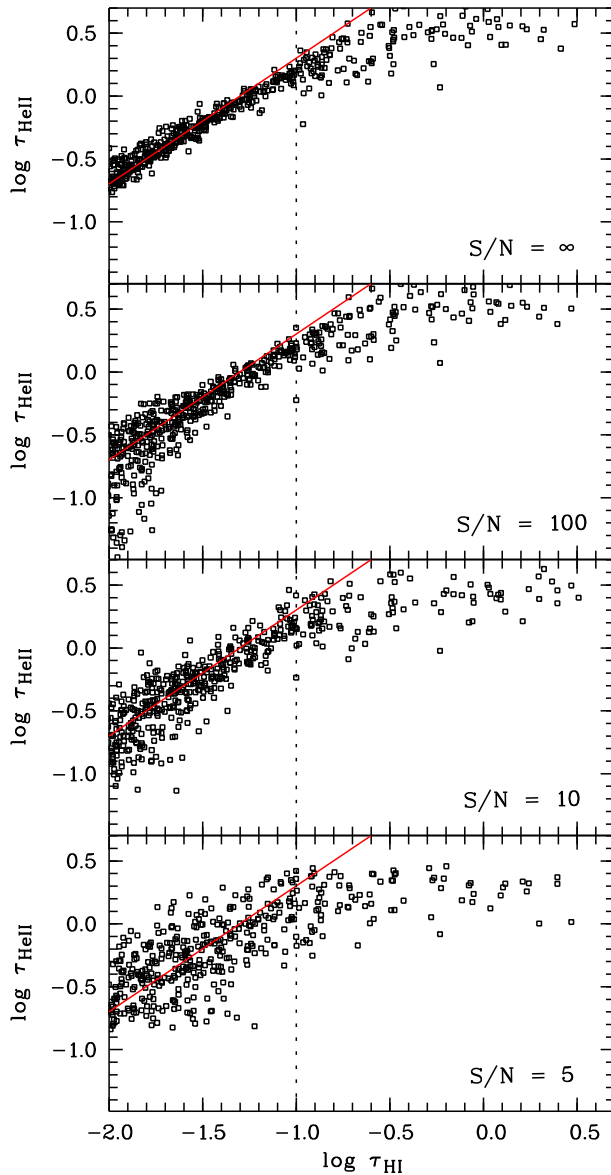


Fig. 8. The He II optical depth versus H I optical depth for simulated data with pure turbulent broadening. The specific signal-to-noise of the artificial helium dataset is given in each panel. The signal-to-noise ratio of the hydrogen spectrum is $S/N = 100$. The upper panel is based on artificial datasets with no noise at all. The resolution of the simulated spectra are $R_{\text{HI}} = 40\,000$ and $R_{\text{HeII}} = 15\,000$, respectively. Each point represents a bin of 20 km s^{-1} . The solid lines indicate $\eta = 80$.

hydrogen optical depths. Thus, a direct comparison of the apparent optical depths above a certain limit is not possible.

Savage & Sembach (1991) give a detailed description of the method and applicability using the apparent optical depth. They emphasize the possibility of finding line saturation in the analysis of line doublets. Hidden saturation can be seen if the apparent column density $N_a(v) \propto \tau_a(v)/f \lambda_0$ of a doublet pair differs with respect to the considered component. Since line saturation is important in the whole FUSE spectrum, the apparent optical depth method is not applicable to bins with

$\tau_{\text{HI}} > 0.1$ if the underlying η is roughly 80. Adopting a 1σ detection limit of $\tau_{\text{HI}} > 0.01$ there is 1 dex of hydrogen optical depth left, allowing the apparent optical depth to be applied reasonably.

Fox et al. (2005) investigated the effect of noise on the apparent column density. They found that the apparent optical depth method will likely overestimate the true column density when applied to data with low S/N . Since the FUSE spectra are very noisy ($S/N \approx 5$), the results obtained by an apparent optical depth method have to be considered carefully.

The bins selected by $-2.0 \leq \log \tau_{\text{HI}} \leq -1.0$ are marked in Fig. 7 and the overlay in the right panels shows their η distribution. Both the samples (pure turbulent and combined line widths) contain virtually no low η values and the fraction of high values is below 5 % in each case. As expected, the mean values approach the underlying η and the scatter decreases. We find $\log \eta_{\text{therm}} = 1.88 \pm 0.24$ and $\log \eta_{\text{turb}} = 1.90 \pm 0.24$, respectively, with a bin size of 20 km s^{-1} . Fitting a Gaussian $A \cdot \exp(-(\log \eta - \log \eta_0)^2/2\sigma^2)$ to the $\log \eta$ distribution of the subsample leads to $\log \eta_0 = 1.90 \pm 0.01$ and $\sigma = 0.237 \pm 0.009$ in the case of pure turbulence. In the case of combined thermal and turbulent broadening we find $\log \eta_0 = 1.89 \pm 0.16$ and $\sigma = 0.213 \pm 0.012$. In comparison to the mean value of the sample without any noise, which is 1.89 ± 0.07 in the pure turbulent case, these values demonstrate that the scatter in the η distribution is mainly due to the noise level of the data. With the present FUSE data ($S/N \sim 5$) an η distribution with a scatter of roughly 13 % can be expected following the simulations.

5.5. Comparing profile fitting and apparent optical depth

The investigation of artificial spectra by fitting Doppler profiles or applying the apparent optical depth method exhibits differences of the robustness and applicability of the diagnostics. Concerning the apparent optical depth, line saturation in combination with the detection limit given by the noise leads to a relatively small interval of 1 dex in the hydrogen optical depth ($0.01 \leq \tau_{\text{HI}} \leq 0.1$), where the method can be applied reliably. Besides limited resolution noise is the most crucial limitation, since measuring the apparent optical depth per velocity bin is directly sensitive to the noise level, while the impact of the assumption of pure turbulent line width is less significant (the deviation is roughly 1 %).

Since position and line width are fixed, noise has less influence using the standard profile-fitting method. Therefore, even saturation is less problematic. Hydrogen starts to be saturated at column densities $\log N_{\text{HI}} \gtrsim 14.5$ and normally higher order Lyman series lines can be used to estimate the H I line parameters accurately in case of strong saturation. Thus, even saturated He II features may be evaluated reasonably. However, in the crowded Ly α forest the number of components may be ambiguous leading to larger uncertainties. Another point is, in analyzing the simulated data, we know that the correct profile function is applied since the datasets are created using it. When dealing with real data, the observed features can be described only approximately.

Table 3. The η values recovered from the simulated data using the profile fitting or apparent optical depth method, respectively. The input value is 80, i.e. $\log \eta = 1.90309$. The first columns show the values for the profile-fitting analysis constraining the sample to $12.0 \leq \log N_{\text{H}\alpha} \leq 13.0$ (selected) and without any restriction (unselected). The columns at the right hand side give the results obtained with the apparent optical depth method (binning 20 km s^{-1}) with $-2.0 \leq \log \tau_{\text{H}\alpha} \leq -1.0$ (selected) and for the total sample (unselected).

| | | profile fitting $\langle \log \eta \rangle$ | apparent optical depth $\langle \log \eta \rangle$ | |
|-----------|------------|--|---|-----------------|
| | | median | median | |
| turbulent | selected | 1.92 ± 0.21 | 1.92 | 1.90 ± 0.24 |
| | unselected | 1.86 ± 0.37 | 1.90 | 1.84 ± 0.41 |
| thermal | selected | 1.85 ± 0.21 | 1.87 | 1.88 ± 0.24 |
| | unselected | 1.77 ± 0.43 | 1.89 | 1.80 ± 0.44 |

A sample restricted to lines that can be clearly identified and are insensitive to effects of thermal broadening is expected to yield the most reliable results. The selected lines have to be strong enough to be fitted unambiguously but are below the sensitivity limit for thermal line widths ($12.0 \leq \log N_{\text{H}\alpha} \leq 14.5$ or even less), since a line sample under the simplistic assumption of pure turbulent broadening will underestimate the true η values. According to Fechner & Reimers (2006) features with $\log N_{\text{H}\alpha} \lesssim 13.0$ remain unaffected by effects of thermal broadening. Therefore a more stringent selection would be $12.0 \leq \log N_{\text{H}\alpha} \leq 13.0$.

Table 3 lists the recovered η values and their statistical 1σ errors using either the profile fitting or the apparent optical depth method. The median reproduces the underlying value of $\log \eta = 1.903$ within an accuracy of more than 93 % in all cases. The statistical mean underestimates the column density ratio fitting line profiles, particularly if thermal broadening is present. This is consistent with the results of Bolton et al. (2006), who come to the conclusion that the median gets closer to the underlying value, although they do not discuss possible reasons for this finding. Furthermore, the scatter is reduced by more than 40 % if only the selected subsamples are considered.

Following these results, we expect to find a scatter in $\log \eta$ of roughly 20 % by analyzing the observed spectra without any further selections. Applying the apparent optical depth method to a subsample with $0.01 \leq \tau_{\text{H}\alpha} \leq 0.1$ leads to a reduced scatter (13 %). For the profile-fitting procedure the scatter can be reduced as well down to about 11 % if only absorbers with $12.0 \leq \log N_{\text{H}\alpha} \leq 13.0$ are selected. This stringent constraint minimizes the effect of systematic underestimation of η if thermal line broadening is present.

6. Results and discussion

Having an idea of the advantages and limitations of the analysis methods, we present applications to the observed data and discuss their implications. In contrast to the simulated data, the ob-

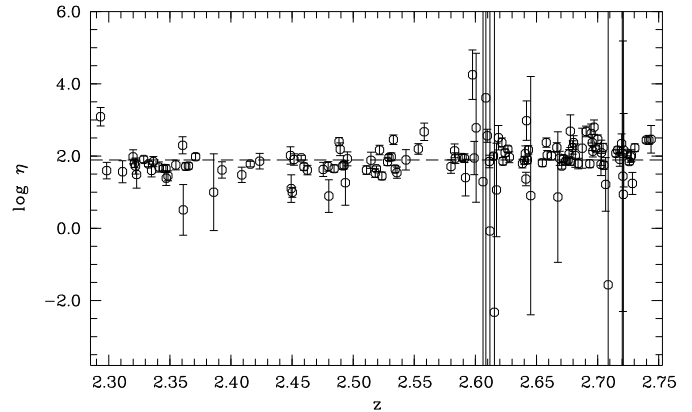


Fig. 9. Redshift distribution of the column density ratio η for absorbers with $12.0 \leq \log N_{\text{H}\alpha} \leq 13.0$. The dashed line indicates the median value $\log \eta = 1.89$.

served spectra contain additional absorption features of metal lines and galactic molecular hydrogen absorption bands. The modelling of this additional absorption, as described in Sect. 4, is considered in the following analyses. In the course of the profile-fitting analysis, the metal line parameters are fixed during the fitting procedure. Using the apparent optical depth method, bins with a metal line or H_2 optical depth $\tau_{\text{met}} > 0.05$ are omitted.

6.1. Profile fitting analysis

In the $\text{He}\alpha$ redshift range covered by FUSE ($z \gtrsim 2.29$) we find 326 $\text{H}\alpha \text{Ly}\alpha$ lines in the Keck spectrum. Due to the FUSE detection gap and terrestrial airglow lines, the number of $\text{H}\alpha$ lines that are supposed to be detectable in $\text{He}\alpha$, reduces to about 300. In addition to the $\text{He}\alpha$ absorbers, which are identified in $\text{H}\alpha$, we have to add several $\text{He}\alpha$ lines without any detected $\text{H}\alpha$ counterparts. These absorbers are about 25 % of all fitted $\text{He}\alpha$ lines. Furthermore, we include the metal absorption lines described in Sect. 4. The resulting distribution of the column density ratio η with redshift is shown in the lower panel of Fig. 4.

Because of the high fraction of lower limits, i.e. $\text{He}\alpha$ features without $\text{H}\alpha$ counterpart, the simple statistical mean of the absorbers with detected $\text{H}\alpha$ and $\text{He}\alpha$ ($\log \eta = 1.54 \pm 1.01$, median 1.72) is expected to be biased. Using the Kaplan-Meier estimator (e.g. Feigelson & Nelson 1985) to derive a mean value including the lower limits yields $\log \eta_{\text{KM}} = 2.13 \pm 0.08$. The median of the total sample is $\log \eta = 1.93$ in good agreement with the results from the studies of the $\text{He}\alpha \text{Ly}\alpha$ forest towards HE 2347-4342 (Kriss et al. 2001; Shull et al. 2004; Zheng et al. 2004b), revealing $\eta \approx 80$.

The values given above are estimated considering the total line sample. As we argue in Sect. 5, more confident results are expected to be found if the line sample is restricted. Therefore, we compute the mean column density ratio considering lines with $12.0 \leq \log N_{\text{H}\alpha} \leq 14.5$ and yield $\log \eta = 1.63 \pm 0.82$ (median 1.72). Since for all $\text{He}\alpha$ features without $\text{H}\alpha$ counterpart the lower limit of the hydrogen column density is less than 10^{12} cm^{-2} , no limits are included in the selected line sample.

Applying the more stringent selection criterion ($12.0 \leq \log N_{\text{H}\text{I}} \leq 13.0$) results in $\log \eta = 1.85 \pm 0.70$ (median 1.89). The redshift distribution of η for this subsample is presented in Fig. 9. Even for the smallest sample the scatter of $\log \eta$ is roughly 40 %. This is significantly more than expected by the simulations. A possible explanation would be the redshift evolution of the column density ratio. Due to the evolution of the sources and absorbers that compose the properties of the UV background, η is expected to change with redshift (e.g. Fardal et al. 1998). Our artificial spectra are generated free from any evolution. Thus, the real data might mimic a higher overall scatter due to redshift evolution. We estimate the column density ratio in different redshift bins of the most stringently selected sample and find indeed an increase of the mean value with redshift. For $z < 2.50$ we yield $\log \eta \approx 1.7$, while $\log \eta \sim 2.0$ is estimated at $z > 2.60$. However, the scatter in each redshift bin is about 20 – 40 %, i.e. part of the scatter in the total redshift range might be due to evolution, but a significant fraction cannot be explained neither by statistical scatter nor by redshift evolution. A Kolmogorov-Smirnov test between the results from the artificial data and the observations yields a probability of less than 1 % for each redshift bin that both samples are based on the same distribution function. This leads to the conclusion that the UV background is indeed fluctuating, even though the results from the profile-fit analysis are insensitive to the scales of the η variation (an attempt to derive these scales is made by Fechner & Reimers 2006).

For investigating the behaviour of η with the hydrogen column density, we concentrate on absorbers with $\log N_{\text{H}\text{I}} < 15.0$. The HI features stronger than this threshold are associated with the LLS in the observed redshift range. Since LLS are believed to arise from material in the outer parts of galaxies, their column density ratio does not probe the ionizing conditions in the IGM but in a galaxy itself. These absorbers are excluded from the sample for the following investigation. Furthermore, we consider only absorbers detected in both HI and HeII with reasonable column density uncertainties $\sigma(\log N_{\text{H}\text{I}, \text{He}\text{II}}) < 1.0$. The distribution of $\log \eta$ with $\log N_{\text{H}\text{I}}$ is shown in the upper panel of Fig. 10. A clear trend is seen, that $\log \eta$ decreases with increasing HI column density. We compute the Spearman rank-order correlation coefficient yielding $r_s = -0.64$. A linear fit to the data $\log \eta = a \cdot \log N_{\text{H}\text{I}} + b$ leads to $a = -0.62 \pm 0.05$ and $b = 9.67 \pm 0.64$.

The analysis of the artificial data (Sect. 5) reveals that a correlation arises if a sample of lines broadened by thermal and turbulent processes is analyzed under the assumption of pure turbulent broadening. The effect is especially noticeable for the column density ratio of absorbers stronger than $\log N(\text{H}\text{I}) \gtrsim 13$, as illustrated in Fig. 6 and discussed in the previous section (see also Fechner & Reimers 2006). In this case we find a Spearman rank coefficient of about -0.25 , while no correlation is found if the assumption of pure turbulent broadening is correct ($r_s \approx 0$). Indeed, the results of Zheng et al. (2004b) imply that the line width is dominated by turbulent broadening, but Fechner & Reimers (2006) have shown that thermal broadening cannot be neglected completely.

Applying the more stringent constraint ($12.0 \leq \log N_{\text{H}\text{I}} \leq 13.0$, presented in the lower panel of Fig. 10) to the observed

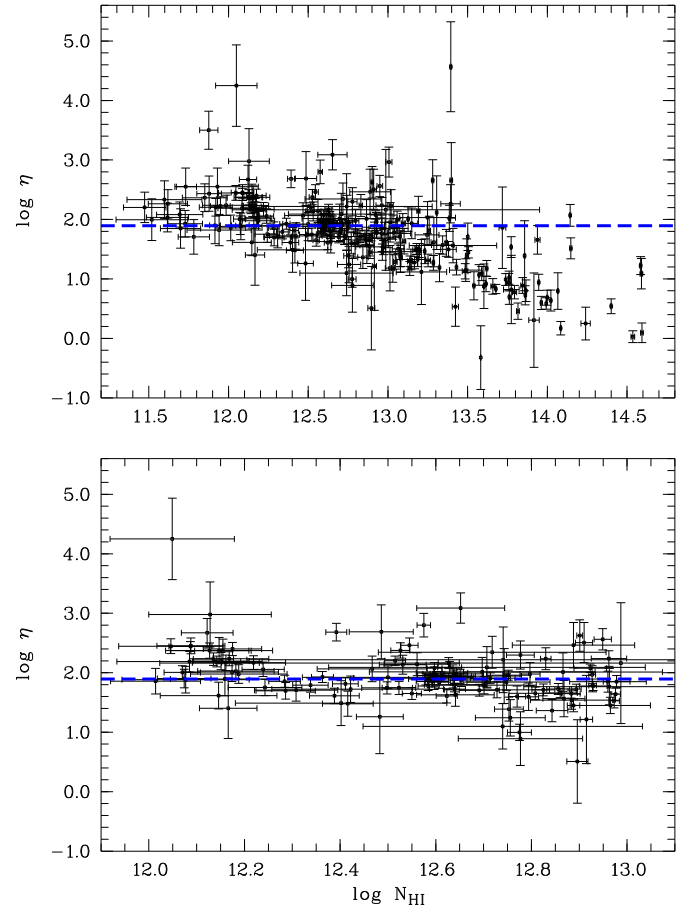


Fig. 10. Distribution of the column density ratio η with hydrogen column density $N_{\text{H}\text{I}}$ (both logarithmic). Only absorbers detected in HI and HeII with $\sigma(\log N_{\text{H}\text{I}, \text{He}\text{II}}) < 1.0$ are shown. The upper panel presents the total sample with $\log N_{\text{H}\text{I}} < 15.0$. The lower panel is a zoom-in to $12.0 \leq \log N_{\text{H}\text{I}} \leq 13.0$. The dashed line represents the median value for the more constrained line sample $\log \eta = 1.89$.

data yields a correlation coefficient $r_s = -0.33$ for the observed sample, which is only half of the value for the larger sample. The linear fit shows now a flatter slope $a = -0.54 \pm 0.13$ and $b = 8.75 \pm 1.66$. Also in this case, the Spearman rank coefficients indicate a slight correlation for the artificial sample with fractional thermal broadening ($r_s \approx -0.2$) and no correlation for the pure turbulent broadened sample. Since we derive a stronger anti-correlation from the observed data compared to the artificial spectra including thermal line widths, the conclusion that η is slightly larger in voids might be correct.

6.2. Apparent optical depth method

Considering the limitations discussed in Sect. 5, we apply the apparent optical depth method to the observed data. In addition, we use the metal line system models of Fechner et al. (2006) with the modifications discussed in Sect. 4 to omit bins which are affected by metal line absorption in the FUSE or the Keck data. Fig. 11 shows the resulting η distribution for both the whole data and the subsample selected by $-2.0 \leq \log \tau_{\text{H}\text{I}} \leq$

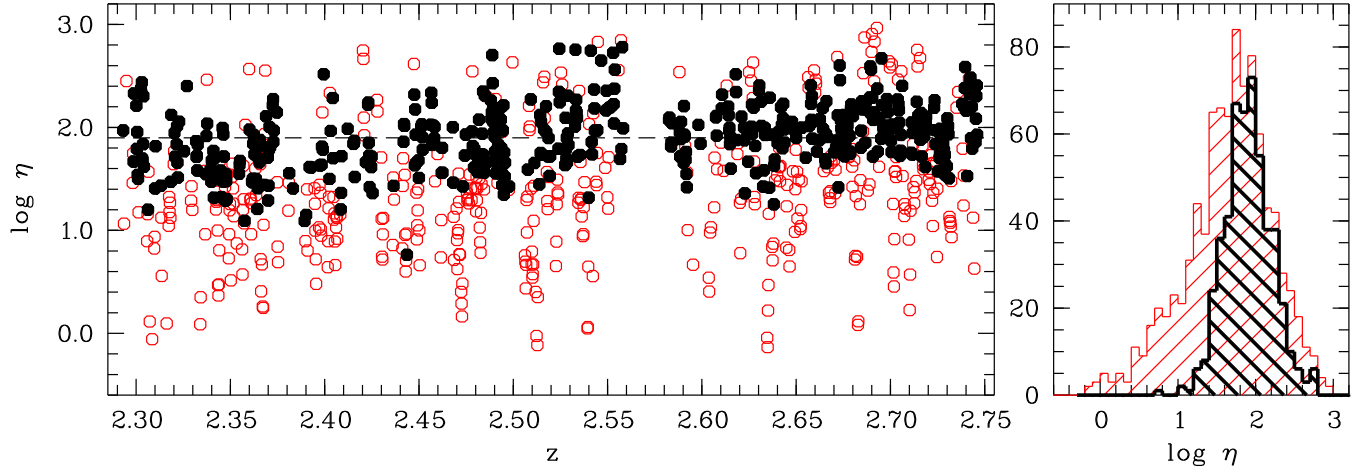


Fig. 11. Distribution of η derived from the observed data of HS 1700+6416 using the apparent optical depth method with a bin size of $\Delta v = 20 \text{ km s}^{-1}$ omitting bins affected by metal line absorption. The selected subsample ($-2.0 \leq \log \tau_{\text{HI}} \leq -1.0$) is indicated as circles and its η distribution is the narrower histogram in the right panel. The dashed line in the left panel represents the median value of the subsample $\log \eta = 1.90$.

-1.0. The subsample consisting of 501 points (54 % of the total sample) only contains values in the range of $1.0 < \log \eta < 3.0$ with a mean value of $\langle \log \eta \rangle = 1.90 \pm 0.30$ (median 1.90). A consideration of the total sample yields $\log \eta = 1.65 \pm 0.55$ and a median of 1.71.

Fitting a Gaussian to the $\log \eta$ distribution of the subsample yields $\log \eta_0 = 1.903 \pm 0.013$ and $\sigma = 0.287 \pm 0.010$ corresponding to $\text{FWHM} = 0.676 \pm 0.023$. The width of the distribution is increased by more than 30 % in comparison to the artificial data. Thus, we may conclude, that in addition to a scatter in η due to noise and saturation effects a physically real variation of η is present.

Figures 11 and 12 show that η is decreasing with redshift. The presented η values are based on the effective optical depth of H I and He II, respectively, per $\Delta z = 0.05$ bin, where censored pixels have been neglected. In the resulting evolution η is rising from $\log \eta = 1.70 \pm 0.32$ at $z \approx 2.33$ up to 1.98 ± 0.32 at $z \approx 2.68$, consistent with the results from the profile-fit analysis. This behaviour of the He II/H I ratio is expected, since it traces the evolution of the ionizing sources. According to Fardal et al. (1998), the observed evolution may be mainly based on a population of quasars with spectral indices $\alpha \sim -1.8$.

An important source of error regarding the redshift evolution of η are the uncertainties in the placement of the continuum in the FUSE spectrum, since the He II optical depth and thus the value of η directly depends on the position of the continuum level. This is also true for the estimate of the column density in case of line-profile fits. As discussed in Sect. 3 the choice of the extinction curve, which is highly uncertain in the EUV, has a strong impact on the continuum level. Especially, if the continuum is extrapolated to a too low level at short wavelengths (e.g. the dotted curve in Fig. 1), the apparent optical depth and consequently the derived η gets too small. Since the extinction law is wavelength-dependent, the uncertainties increase with decreasing wavelength. Additionally, the inaccurate definition of the zero flux level at short wavelengths results in systemati-

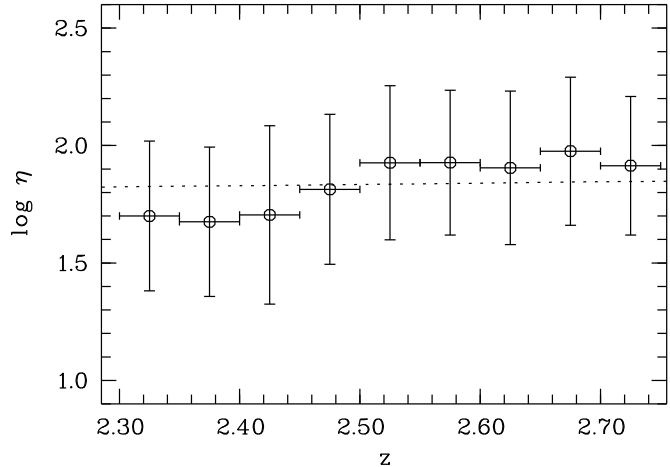


Fig. 12. Evolution of η with redshift. The dotted curve represents the expected values if the ionizing sources are quasars with a spectral index of $\alpha = -1.8$ as modelled by Fardal et al. (1998).

cally underestimated He II optical depths leading to low η values. Thus, it might be an artifact from the continuum definition and/or zero flux level estimation that the observed evolution of $\log \eta$ appears to be steeper than predicted by the model of Fardal et al. (1998). However, Zheng et al. (2004b) find a very similar evolution towards HE 2347-4342, a line of sight with a lower extinction ($E(B-V) = 0.014$).

A correlation between the H I optical depth and the He II/H I ratio is still present in the subsample. The Spearman rank-order coefficient for this correlation is $r_s = -0.53$. However, also the subsamples of the artificial datasets show slight correlations leading to $r_s \approx -0.36$ for both broadening mechanisms. The slope describing the observed sample ($a = -0.66 \pm 0.04$) is roughly twice as steep as those from the simulated datasets with uncertainties of the same order of magnitude. This is consistent

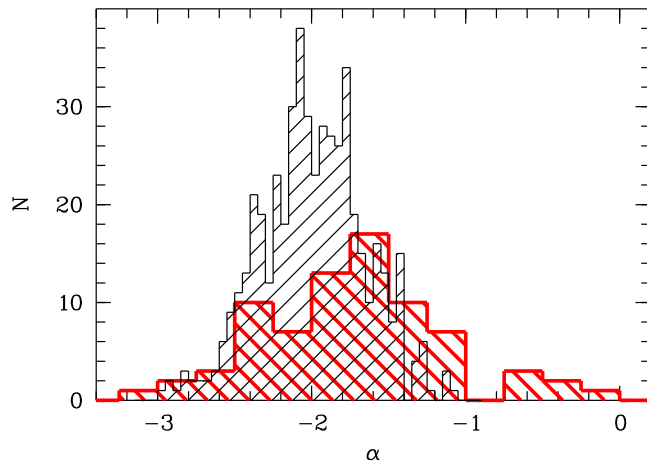


Fig. 13. Distribution of the spectral indices α (used as $f_\nu \propto \nu^\alpha$) for the observed sample (derived from the apparent optical depth result; thin line) and the whole sample from Telfer et al. (2002, larger bin size, thick line). The observed spectral indices are derived from the measured η values using the correlation illustrated as Model A2 in Fig. 10 of Fardal et al. (1998). Different bin sizes are used for a better presentation.

with the results from the profile-fit analysis discussed in detail in the previous Section. We therefore confirm the conclusion that part of the correlation between H I voids and high η values might be real.

6.3. The ionizing background

Summarizing the results obtained by applying the apparent optical depth method and the profile-fitting procedure, we find a mean value of the column density ratio $\log \eta = 1.90$ (corresponding to $\eta \approx 80$). The observed scatter is larger than expected from the analysis of artificial data. Part of the enhanced scatter is possibly due to evolution of the column density ratio with redshift, which has not been incorporated in the artificial data. Measuring η and its scatter in smaller redshift bins suggests as well that part of the scatter must be attributed to physical effects beyond statistical noise.

The origin of the scatter must be related to fluctuations in the He II ionizing radiation since the photoionization rate of H I can be assumed to be uniform (a more detailed argumentation is given by e.g. Bolton et al. 2006). Spatial variation at the He II ionization edge may be due to the wide range of spectral indices of the energy distribution of quasars (Zheng et al. 1997; Telfer et al. 2002; Scott et al. 2004). Shull et al. (2004) and Zheng et al. (2004b) compared the estimated column density ratios towards HE 2347-4342 to the distribution of the spectral indices α of 79 quasars presented by Telfer et al. (2002). Both found an excess of softer radiation. Fig. 13 shows the distribution of α derived from the observed subsample applying the apparent optical depth method. The η values are converted into spectral indices using the relation between the He II/H I ratio and the source's spectral index presented by Fardal et al. (1998, their Fig. 10, Model A2). As a mean spec-

tral index, we find $\langle \alpha \rangle = -1.99 \pm 0.34$. In comparison to the total sample of Telfer et al. (2002), we confirm the excess of softer spectral indices. One should keep in mind that the conversion from η into α is based on a phenomenological model, which certainly contains additional sources of error.

Following the arguments of Shull et al. (2004), it is possible to convert the η values directly into effective spectral indices. The effective spectral index α_{eff} describes the radiation an absorber is directly exposed to rather than the radiation once emitted by the sources, i.e. it denotes the spectral index of the filtered radiation of the sources. Assuming a temperature of $T = 10^{4.3}$ K and the equality of the local spectral indices at 1 and 4 Ryd, respectively, leads to $\eta = 1.70 \cdot 4^{-\alpha_{\text{eff}}}$ (for details see Shull et al. (2004) and references therein). Applying this relation the α distribution is broader and shifted to even softer indices: $\langle \alpha_{\text{eff}} \rangle = -2.78 \pm 0.50$. The results from the profile-fitting method lead to similar numbers.

Bolton et al. (2006) have studied the observed spatial variation of the column density ratio arising from a fluctuating UV background. According to their model, the fluctuations are based on variations in the He II photoionization rate due to properties of the emitting quasars, such as the spatial distribution, luminosity function, and the spectral energy distribution (see also Fardal et al. 1998). Bolton et al. (2006) find η values scattered over 2 dex roughly consistent with the results from Zheng et al. (2004b), but failed to reproduce a significant number of points with $\eta < 10$. As discussed in the previous Sections, the results from the line profile-fitting procedure are likely to be biased due to thermal line broadening when considering high density absorbers (see also Fechner & Reimers 2006). Although Bolton et al. (2006) do not address this problem their Fig. 4 reveals an increased number of lines with a low column ratio for increasing H I column density. Considering only absorbers in a restricted column density range eliminates most of the points with very low η (see Figs. 9 and 11). We conclude that there are no absorbers exposed to radiation harder than those emitted by QSOs. Thus, the column density ratios inferred from the data of HS 1700+6416 support the model proposed by Bolton et al. (2006) to explain the spatial fluctuation of the column density ratio.

Apart from scatter, the average value of the column density ratio can be roughly related to the dominating sources of ionizing radiation. The inferred value ($\eta \approx 80$) is in very good agreement with the results towards HE 2347-4342 (Kriss et al. 2001; Shull et al. 2004; Zheng et al. 2004b). It is consistent with the UV background of Haardt & Madau (2001) based on QSOs only. However, there is growing evidence that there are contributions to the ionizing background from other sources than quasars (e.g. Heap et al. 2000; Smette et al. 2002; Aguirre et al. 2004; Bolton et al. 2006; Kirkman et al. 2005). The excess of soft spectral indices found from Fig. 13 suggests that part of the absorbers are indeed exposed to softer radiation.

Our data reduction may still be in need of improvement concerning the zero flux level (see Sect. 2). This is in particular true for shorter wavelengths. In order to exclude possible biases due to the reduction problems, we estimate the mean column density ratio for wavelengths longer than 1086 Å ($z > 2.58$), where the data reduction appears to be correct. We

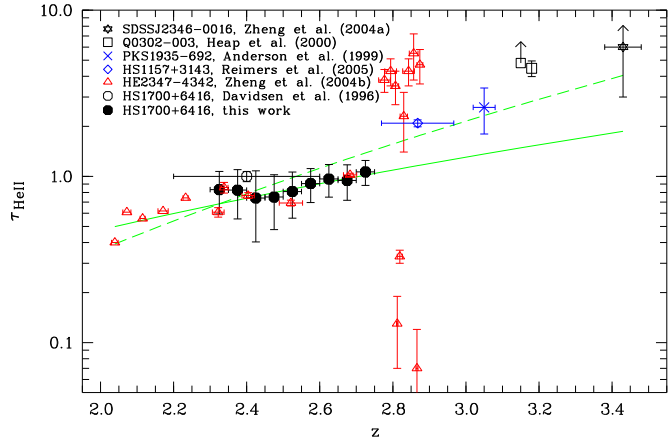


Fig. 14. Evolution of the He II opacity with redshift. In addition to the opacities measured in this work (filled circles), values measured towards five additional QSOs with detected He II absorption are shown. The solid curve represents the relation $\tau_{\text{He II}} \propto (1+z)^{3.5}$ (Fardal et al. 1998) fitted to the data points $z < 2.75$. The dashed line indicates an overall fit to the data resulting in $\tau_{\text{He II}} \propto (1+z)^{6.2 \pm 0.4}$.

find a median of $\log \eta = 2.01$ adopting the profile-fitting results and a slightly lower value (≈ 1.97) using the apparent optical depth method. These values ($\eta \approx 93 \dots 102$) are consistent with predictions for the UV background including also young star forming galaxies (Haardt & Madau 2001) and in the same range as predicted by the models of Bolton et al. (2006) at the same redshift based on a modified version of the UV background of Madau et al. (1999).

6.4. Redshift evolution of the He II optical depth

Fig. 14 shows a compilation of the measured He II opacity $\tau_{\text{He II}}$ from the literature (Davidsen et al. 1996; Anderson et al. 1999; Heap et al. 2000; Zheng et al. 2004a,b; Reimers et al. 2005a) together with our measurements from the FUSE spectrum of HS 1700+6416 (filled circles). Estimating the mean normalized flux per redshift bin, pixels affected by metal line absorption are excluded. We find a mild evolution from $\tau_{\text{He II}} = 0.83 \pm 0.24$ at $z = 2.30 - 2.35$ to 1.06 ± 0.18 at $z = 2.70 - 2.75$ with a slight dip (0.74 ± 0.34) at $z \approx 2.45$. These values are consistent with the opacity measurements towards HE 2347-4342 in the same redshift range (Zheng et al. 2004b).

Davidsen et al. (1996) estimated $\tau_{\text{He II}} = 1.00 \pm 0.07$ at $\langle z \rangle = 2.4$ using a low resolution spectrum taken with the Hopkins Ultraviolet Telescope (HUT). As can be seen from Fig. 14 our values are systematically lower by about 25 %. Tests with the data uncorrected for metal line absorption suggest that this difference is partly due to the additional absorption by metal lines raising the opacity by roughly 10 %. Additionally, differences in the continuum level may account for the higher effective optical depth derived by Davidsen et al. (1996). However, the values are consistent on the 1σ level.

The solid line in Fig. 14 represents the relation $\tau_{\text{He II}} \propto (z+1)^{3.5}$ (Fardal et al. 1998) providing a suitable fit to the data

at $z < 2.75$. The value of the power law exponent $\gamma + 1$ is chosen according to the results from H I Ly α forest statistics (e.g. Press et al. 1993; Kim et al. 2002). Deviations from this relation at higher redshift are commonly interpreted as the evidence for the tail end of the epoch of He II reionization which completes at $z \sim 2.8$ (e.g. Reimers et al. 1997; Kriss et al. 2001; Zheng et al. 2004b). At $z > 3$ very high values of the He II optical depth can be detected. A simple overall fit to all data points would lead to $\tau_{\text{He II}} = 4.0 \cdot 10^{-4} (z+1)^{6.2 \pm 0.4}$ (dashed line in Fig. 14). This fit should not be interpreted as a reasonable model for the evolution of $\tau_{\text{He II}}$.

7. Summary and conclusions

We have presented far-UV data of the quasar HS 1700+6416 taken with FUSE, which is the second line of sight permitting us to resolve the He II Ly α forest. The data are of comparable quality ($S/N \sim 5$, $R \approx 20\,000$) to those of HE 2347-4342 and cover the redshift range $2.29 \leq z \leq 2.75$. In this redshift range, no strong variations of the He II opacity are detected. The evolution of the effective optical depth is consistent with $(z+1)^{3.5}$, i.e. this line of sight probes the post-reionization phase of He II.

The column density ratio η has been derived using line profile fits and the apparent optical depth method, respectively. A preliminary study of simple artificial spectra created on the basis of the statistical properties of the Ly α forest including or neglecting thermal line broadening, respectively, reveals the shortcomings of the standard analysis methods. The reasons are noise, line saturation, and effects due to the assumption of pure turbulence if thermal broadening contributes to the line widths. We find that the profile-fitting procedure leads to reliable results only for absorbers with H I column densities in the range $12.0 \leq \log N_{\text{H I}} \leq 13.0$. The apparent optical depth method is only valid in the range $0.01 \leq \tau_{\text{H I}} \leq 0.1$. Otherwise, η would be underestimated in the case of strong H I absorption. Furthermore, a scatter in η of 10 – 15 % is expected even if the underlying value is constant.

In order to avoid systematic biases due to additional absorption in the He II Ly α forest, a model of the metal line features expected to arise in the FUSE spectral range (Fechner et al. 2006) has been included in the analysis. We have also considered features of galactic H₂ absorption. 27 % of all fitted He II lines are affected by metal lines, in case of 19 % of the lines the derived η value changes significantly, i.e. by more than $\Delta \log \eta = 0.01$. Additionally, the required number of He II absorbers without detectable H I counterpart is reduced by 30 % if metal lines are taken into account, and the average η value slightly decreases. Although the consideration of metal line absorption does not distort strongly the statistical properties of the resulting η distribution, individual values could have been biased by up to an order of magnitude.

Photoionization models of the absorbers showing associated metal lines provide an independent estimate of η . For these systems the He II column density can be computed based on the photoionization model for the metal line features. Comparing the η values directly measured from the profile-fitting procedure and inferred from the metal line system modelling leads in principle to consistent results. A more detailed discussion will

be given in a future paper (Fechner & Reimers 2006) which will also discuss the absence of the He II proximity effect towards this QSO.

For the redshift range $2.58 \leq z \leq 2.75$, where the spectrum appears to be free of artifacts due to the reduction process, the data reveals $\log \eta \approx 2.0$ on average. This value ($\eta \approx 100$) indicates a contribution of galaxies to the UV background at these redshifts, consistent with current results from studies of the H I opacity and the metallicity of the IGM.

The scatter of η is larger than expected compared to our analysis of artificial datasets. Therefore, we infer that the UV background might really fluctuate, even though our present results are insensitive to amplitude and scale of these variations. The main limiting factor for a quantitative estimate of the fluctuations is the high noise level of the data. Converting the values of the column density ratio into spectral indices, we confirm the apparent excess of soft sources as found by Shull et al. (2004) and Zheng et al. (2004b). Our results suggest, that the apparent correlation between the η value and the strength of the H I absorption may be an artifact of the analysis method and does not reflect physical reality.

Since we have shown that the assumption of pure turbulent line broadening will lead to systematical errors, the next step in the analysis of the resolved He II Ly α forest should be to avoid this assumption. The apparent optical depth method applied to an appropriately restricted sample should lead to unbiased results independent of the dominant line broadening mechanism. A bin by bin comparison as performed by the apparent optical depth method provides little potential for taking into account a potentially dominant thermal broadening, while the profile-fitting procedure could drop the assumption of pure turbulence. However, obtaining reasonable fits would be more challenging due to the low S/N of the data. This would provide an independent strategy to estimate the IGM temperature.

Acknowledgements. This work is based on data obtained as part of FUSE guest investigator proposal C123, and on data obtained for the Guaranteed Time Team by the NASA-CNES-CSA FUSE mission operated by the Johns Hopkins University. Financial support to U. S. participants has been provided by NASA contract NAS5-32985. We thank the FUSE Science and Operations team at JHU for their special efforts to schedule additional observations in the spring of 2003 and in coordination with the NASA/ESA Hubble Space Telescope. The HST observations were obtained at the Space Telescope Science Institute, which is operated by the Association of Universities for Research in Astronomy, Inc., under NASA contract NAS 5-26555. These observations are associated with program #9982. CF has been supported by the Verbundforschung (DLR) of the BMBF under Grant No. 50 OR 0203 and by the DFG under RE 353/49-1.

References

Abgrall, H., Roueff, E., Launay, F., Roncin, J. Y., & Subtil, J. L. 1993a, A&AS, 101, 273

Abgrall, H., Roueff, E., Launay, F., Roncin, J. Y., & Subtil, J. L. 1993b, A&AS, 101, 323

Agafonova, I. I., Centurión, M., Levshakov, S. A., & Molaro, P. 2005, A&A, 441, 9

Aguirre, A., Schaye, J., Kim, T., et al. 2004, ApJ, 602, 38

Anderson, S. F., Hogan, C. J., Williams, B. F., & Carswell, R. F. 1999, AJ, 117, 56

Bianchi, S., Cristiani, S., & Kim, T.-S. 2001, A&A, 376, 1

Bolton, J. S., Haehnelt, M. G., Viel, M., & Carswell, R. F. 2006, MNRAS, 366, 1378

Bruzual A., G. & Charlot, S. 1993, ApJ, 405, 538

Cardelli, J. A., Clayton, G. C., & Mathis, J. S. 1989, ApJ, 345, 245

Davidson, A. F., Kriss, G. A., & Zheng, W. 1996, Nature, 380, 47

Diplas, A. & Savage, B. D. 1994, ApJ, 427, 274

Fardal, M. A., Giroux, M. L., & Shull, J. M. 1998, AJ, 115, 2206

Fechner, C. & Reimers, D. 2006, A&A, submitted

Fechner, C., Reimers, D., Songaila, A., et al. 2006, A&A, submitted

Feigelson, E. D. & Nelson, P. I. 1985, ApJ, 293, 192

Fox, A. J., Savage, B. D., & Wakker, B. P. 2005, AJ, 130, 2418

Haardt, F. & Madau, P. 1996, ApJ, 461, 20

Haardt, F. & Madau, P. 2001, in Clusters of Galaxies and the High Redshift Universe Observed in X-rays, ed. D. M. Neumann & J. T. T. Van, 64

Heap, S. R., Williger, G. M., Smette, A., et al. 2000, ApJ, 534, 69

Hu, E. M., Kim, T., Cowie, L. L., Songaila, A., & Rauch, M. 1995, AJ, 110, 1526

Jakobsen, P., Boksenberg, A., Deharveng, J. M., et al. 1994, Nature, 370, 35

Köhler, S., Reimers, D., & Wamsteker, W. 1996, A&A, 312, 33

Kim, T.-S., Carswell, R. F., Cristiani, S., D'Odorico, S., & Giallongo, E. 2002, MNRAS, 335, 555

Kirkman, D. & Tytler, D. 1997, ApJ, 484, 672

Kirkman, D., Tytler, D., Suzuki, N., et al. 2005, MNRAS, 360, 1373

Kriss, G. A., Shull, J. M., Oegerle, W., et al. 2001, Science, 293, 1112

Madau, P., Haardt, F., & Rees, M. J. 1999, ApJ, 514, 648

McCandliss, S. R. 2003, PASP, 115, 651

Miralda-Escudé, J. 1993, MNRAS, 262, 273

Miralda-Escudé, J. 2005, ApJ, 620, L91

Misawa, T. 2002, PhD thesis, University of Tokyo

Møller, P. & Jakobsen, P. 1990, A&A, 228, 299

Moos, H. W., Cash, W. C., Cowie, L. L., et al. 2000, ApJ, 538, L1

Pei, Y. C. 1992, ApJ, 395, 130

Petitjean, P., Riediger, R., & Rauch, M. 1996, A&A, 307, 417

Picard, A. & Jakobsen, P. 1993, A&A, 276, 331

Press, W. H., Rybicki, G. B., & Schneider, D. P. 1993, ApJ, 414, 64

Reimers, D., Bade, N., Schartel, N., et al. 1995, A&A, 296, L49

Reimers, D., Fechner, C., Hagen, H.-J., et al. 2005a, A&A, 442, 63

Reimers, D., Hagen, H.-J., Schramm, J., Kriss, G. A., & Shull, J. M. 2005b, A&A, 436, 465

Reimers, D., Köhler, S., Wisotzki, L., et al. 1997, A&A, 327, 890

Reimers, D., Vogel, S., Hagen, H.-J., et al. 1992, *Nature*, 360, 561

Richter, P., Sembach, K. R., Wakker, B. P., & Savage, B. D. 2001, *ApJ*, 562, L181

Richter, P., Wakker, B. P., Savage, B. D., & Sembach, K. R. 2003, *ApJ*, 586, 230

Ricotti, M., Gnedin, N. Y., & Shull, J. M. 2000, *ApJ*, 534, 41

Sahnow, D. J., Moos, H. W., Ake, T. B., et al. 2000, *ApJ*, 538, L7

Savage, B. D. & Sembach, K. R. 1991, *ApJ*, 379, 245

Schaye, J. 2004, *ApJ*, submitted, astro-ph/0409137

Schlegel, D. J., Finkbeiner, D. P., & Davis, M. 1998, *ApJ*, 500, 525

Scott, J., Bechtold, J., Dobrzycki, A., & Kulkarni, V. P. 2000, *ApJS*, 130, 67

Scott, J. E., Kriss, G. A., Brotherton, M., et al. 2004, *ApJ*, 615, 135

Shull, J. M., Tumlinson, J., Giroux, M. L., Kriss, G. A., & Reimers, D. 2004, *ApJ*, 600, 570

Simcoe, R. A., Sargent, W. L. W., & Rauch, M. 2002, *ApJ*, 578, 737

Simcoe, R. A., Sargent, W. L. W., Rauch, M., & Becker, G. 2006, *ApJ*, 637, 648

Smette, A., Heap, S. R., Williger, G. M., et al. 2002, *ApJ*, 564, 542

Songaila, A. 1998, *AJ*, 115, 2184

Telfer, R. C., Zheng, W., Kriss, G. A., & Davidsen, A. F. 2002, *ApJ*, 565, 773

Tripp, T. M., Lu, L., & Savage, B. D. 1997, *ApJS*, 112, 1

Vogel, S. & Reimers, D. 1993, *A&A*, 274, L5

Vogel, S. & Reimers, D. 1995, *A&A*, 294, 377

Zhang, Y., Anninos, P., Norman, M. L., & Meiksin, A. 1997, *ApJ*, 485, 496

Zheng, W., Chiu, K., Anderson, S. F., et al. 2004a, *AJ*, 127, 656

Zheng, W., Kriss, G. A., Deharveng, J.-M., et al. 2004b, *ApJ*, 605, 631

Zheng, W., Kriss, G. A., Telfer, R. C., Grimes, J. P., & Davidsen, A. F. 1997, *ApJ*, 475, 469